J. Fluid Mech. (2014), *vol.* 747, *pp.* 73–102.
doi:10.1017/jfm.2014.154

Turbulent flow in the bulk of Rayleigh–Bénard convection: aspect-ratio dependence of the small-scale properties

Matthias Kaczorowski, Kai-Leong Chong and Ke-Qing Xia†

Department of Physics, The Chinese University of Hong Kong, Shatin, Hong Kong, China

(Received 16 July 2013; revised 27 February 2014; accepted 17 March 2014;
first published online 10 April 2014)

Geometrical confinement of turbulent Rayleigh–Bénard convection (RBC) in Cartesian geometries is found to reduce the local Bolgiano length scale in the centre of the cell $L_{B,centre}$ and can therefore be used to study cascade processes in the bulk of RBC. The dependence of $L_{B,centre}$ versus Γ suggests a cut-off to the local L_B, which depends on the Prandtl number Pr and is of the order of the cell's smallest dimension. It is also observed that geometrical confinement changes the topology of the flow, causing the turbulent kinetic energy dissipation rate and the temperature variance dissipation rate (averaged over the centre of the cell and normalized by their respective global averages) to exhibit a maximum at a certain Γ, which roughly coincides with the aspect ratio at which the viscous and thermal boundary layers of the two opposite lateral walls merge. As a result the mean heat flux through the core region also exhibits a maximum. Unlike in the cubic case, we find that geometrical confinement of the flow results in a local balance of the heat flux and the turbulent kinetic energy dissipation rate for $Pr = 4.38$ for all values of the Rayleigh number Ra (up to 10^{10}), while no balance is observed for $Pr = 0.7$. The need for very high bulk resolution to accurately resolve the gradients of the flow field at high Ra is shown by analysing the second-order structure functions of the vertical velocity and temperature in the bulk of RBC. Under-resolution of the temperature field yields a large error in the dissipative range scaling, which is believed to be an effect of intermittently penetrating thermal plumes. The resolution contrast resulting from the requirement to resolve the thermal plumes and the homogeneous and isotropic background turbulence scales as $\delta_T/\langle\eta_k\rangle_{centre} \sim Ra^{0.1}$ and should therefore be taken into account when tackling very high Ra. In the case studied here, under-resolution can have a significant effect on the local heat flux through the centre of the cell.

Key words: Bénard convection, turbulent convection, turbulence simulation

1. Introduction

Turbulent thermal convection in a Rayleigh–Bénard configuration has been a very active area of research in the past two decades (Ahlers, Grossmann & Lohse 2009; Lohse & Xia 2010; Chillà & Schumacher 2012; Xia 2013). However, the question of

† Email address for correspondence: kxia@phy.cuhk.edu.hk

how the small-scale properties of the convective flow depend on the aspect ratio has not been investigated systematically. Such a study could shed light on how various quantities behave as the system crosses over from being three-dimensional (3-D) to being 2-D/quasi-2-D. In Kaczorowski & Xia (2013) we asked questions on how the local Bolgiano length scale varies with the Rayleigh number Ra for the Prandtl numbers $Pr = 0.7$ and $Pr = 4.38$, how this scaling compares with the scaling of the global estimate of the Bolgiano length scale and how this is reflected in the structure functions in the bulk of turbulent Rayleigh–Bénard convection (RBC) in a cubic geometry. We found that the local Bolgiano length scale in the bulk is not only much larger than the global estimate of the Bolgiano length scale, but also increases rapidly after a certain critical Rayleigh number, which depends on the Prandtl number and appears to grow as the Prandtl number increases. Thus, we took into account two important parameters that govern the flow, namely the Rayleigh number $Ra = \alpha g W_z^3 \Delta T/(\nu\kappa)$ and the Prandtl number $Pr = \nu/\kappa$, where α, ν and κ are the thermal expansion coefficient, kinematic viscosity and thermal diffusivity of the convecting fluid, respectively, and g is the gravitational acceleration. The height of the fluid layer is given by W_z and the temperature difference between the horizontal top and bottom plates is ΔT.

A third parameter that is interesting to study, but which is not easy to vary experimentally over a wide range and might require significant computational resources for its large values, is the aspect ratio Γ of the container. The impact of the aspect ratio of a cylindrical cell on the thickness of the horizontal and vertical boundary-layer thicknesses was theoretically investigated by Grossmann & Lohse (2003). The aspect-ratio dependence of the heat transfer has been experimentally investigated by Funfschilling *et al.* (2005) and by Sun *et al.* (2005*a*) using a cylindrical cell with aspect ratios $0.67 \leqslant \Gamma \leqslant 20$. It was found that the heat transfer reaches its large-Γ asymptotic value for $\Gamma \geqslant 10$. The influence of the aspect ratio ($0.25 \leqslant \Gamma \leqslant 12$) of a cylindrical cell on the heat transfer was numerically investigated by Bailon-Cuba, Emran & Schumacher (2010) for $10^7 \leqslant Ra \leqslant 10^9$ and $Pr = 0.7$. They observed that the Γ scaling of the heat transfer has a local minimum for $\Gamma \approx 2.5$, which coincides with a change from a single- to a double-role structure. They also observed that the contribution of the primary proper orthogonal decomposition mode, which is associated with the large-scale circulation (LSC), to the heat transport increases with Γ. The influence of the aspect ratio ($0.23 \leqslant \Gamma \leqslant 13$) on the flow structure of two-dimensional RBC ($10^7 \leqslant Ra \leqslant 10^{12}$ and different Pr of order unity) was also investigated by Poel *et al.* (2012). They show that finite size effects gradually vanish as the aspect ratio is increased and appear to be negligible for $\Gamma > 10$. They also investigate the influence of different experimentally observed flow states (Roche *et al.* 2002; Funfschilling, Bodenschatz & Ahlers 2009; Niemela & Sreenivasan 2010) on the global heat transfer, in order to understand how these flow states affect the heat transfer efficiency Nu–Ra scaling, where Nu is the Nusselt number. Using a rectangular water-filled geometry consisting of 50 cm × 15 cm horizontal plates and sidewalls of varying heights with 2.4 cm $\leqslant H \leqslant$ 40 cm Zhou *et al.* (2012) observed that the global heat transfer is not affected by the aspect ratio of the container, which they concluded to be an effect of the different dynamics of the large-scale flow as compared to cylindrical geometries. Recently, in an experimental and numerical study Huang *et al.* (2013) found that the heat transfer efficiency Nu can be significantly enhanced (∼20 %) when the aspect ratio Γ is reduced to be less than one, i.e. when the system is changed from a cube to a narrow rectangle. This geometrical confinement-induced heat transfer enhancement was shown to result from

the changes in the dynamics and morphology of the thermal plumes in the boundary layers and in the large-scale flow structures in the bulk (Huang *et al.* 2013).

In contrast to studies of the global properties of the flow, there are many fewer investigations of the local quantities. One of the interesting questions is how, and how much, heat is transferred through the bulk of the flow (Shishkina & Wagner 2006, 2007; Kaczorowski & Wagner 2009; Emran & Schumacher 2012). Another interesting property is the Bolgiano length scale, at which a cross-over from buoyancy- to inertia-dominated cascade dynamics occurs, which has been studied by numerous authors (e.g. Ching 2000; Shang & Xia 2001; Zhou & Xia 2001; Calzavarini, Toschi & Tripiccione 2002; Sun, Zhou & Xia 2006; Kunnen *et al.* 2008; Zhou & Xia 2008; He, Tong & Ching 2010; Lohse & Xia 2010). From their recent study of Rayleigh–Taylor turbulence Boffetta *et al.* (2012) concluded that the smallest length of the geometry can be used to confine the Bolgiano length scale, so that cascade processes in turbulent thermal convection may be studied by varying the aspect ratio of the cell. Geometrical confinement of turbulent flows was also studied by Celani, Musacchio & Vincenzi (2010), who found that reduction of the dimensionality of a system, and hence the forcing length scale, leads to a cascade splitting with a direct cascade below and an indirect cascade above the forcing length scale. Boffetta *et al.* (2012) show that the Bolgiano length scale in their simulations of Rayleigh–Taylor turbulence is associated with an indirect cascade. In light of this observation we now analyse the impact of the aspect ratio of a Cartesian geometry on the flow in the bulk of turbulent RBC.

In this paper we use direct numerical simulations of RBC in Cartesian geometries with different lateral aspect ratios in order to answer the question of how the local Bolgiano length scale is affected by the aspect ratio and whether the lateral confinement would be a useful tuning parameter to study cascade processes in the bulk of RBC. Furthermore, we extract the local heat flux in the centre of these cells and compare the results with our previous findings for a cube and the experimental results for a cylindrical cell obtained by Ni, Huang & Xia (2011). Using the example of an aspect ratio $\Gamma = 1/4$ geometry filled with water and $Ra = 1 \times 10^{10}$ we also study the influence of the resolution in the bulk on the dynamics of the flow in this region.

2. Numerical set-up

In § 2.1 we briefly describe the governing equations and the numerical method used, while § 2.2 explains the geometries and meshes used in the present study and provides a list of the relevant simulation parameters.

2.1. *Numerical method*

We solve the non-dimensional governing equations (Kaczorowski & Xia 2013)

$$\left.\begin{aligned} &\boldsymbol{\nabla}\cdot\boldsymbol{u} = 0,\\ &\partial\boldsymbol{u}/\partial t + \boldsymbol{u}\cdot\boldsymbol{\nabla}\boldsymbol{u} + \boldsymbol{\nabla}p = (Ra/Pr)^{-1/2}\Delta\boldsymbol{u} + T\boldsymbol{e}_z,\\ &\partial T/\partial t + \boldsymbol{u}\cdot\boldsymbol{\nabla}T = (RaPr)^{-1/2}\Delta T \end{aligned}\right\} \tag{2.1}$$

using a fourth-order accurate finite volume method, where $\boldsymbol{u} = (u, v, w)$ is the velocity vector, and T and p represent the temperature and pressure, respectively. The gravity vector is acting in the vertical direction, i.e. the $-\boldsymbol{e}_z$ direction. For a more complete description of the numerical method used and a comparison of the *Nu*–*Ra* scaling with

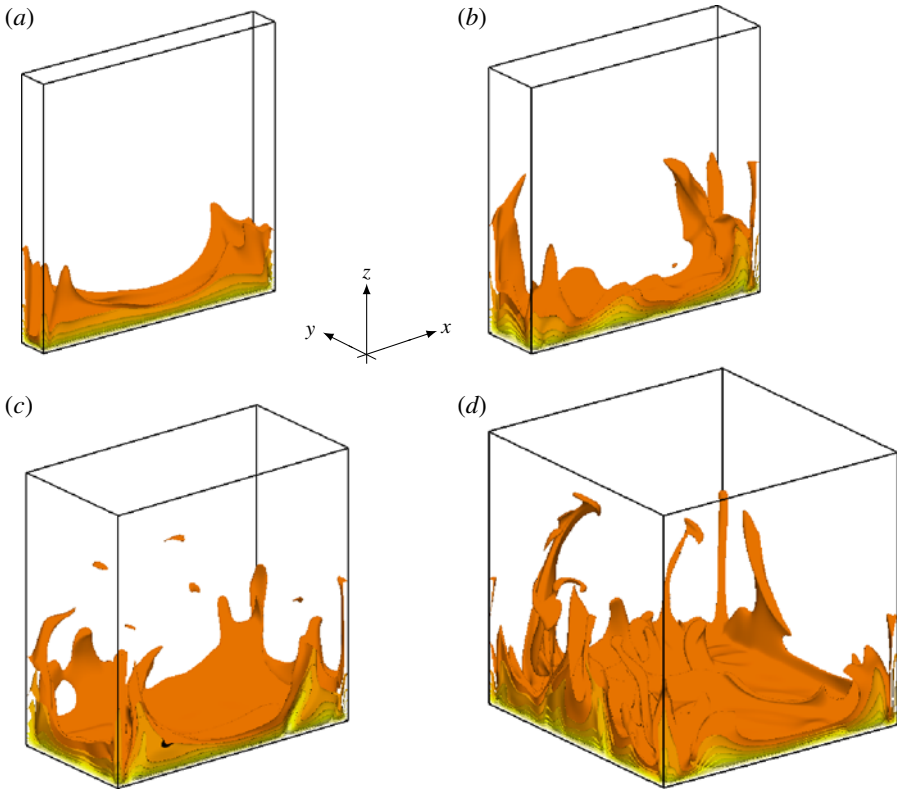

FIGURE 1. (Colour online) Illustration of the rectangular geometries with four different aspect ratios, (*a*) $\Gamma = 1/8$, (*b*) $\Gamma = 1/4$, (*c*) $\Gamma = 1/2$ and (*d*) $\Gamma = 1$, and a visualization of the instantaneous temperature field with isosurfaces for $T \geqslant 0.1$ to give an impression of the size of the large coherent structures ($Ra = 10^8$ and $Pr = 4.38$). The colour scale is from white (hot plate) through yellow to orange (bulk flow).

experimental data the reader is referred to Kaczorowski & Xia (2013). A comparison with experimental data can also be found in Huang *et al.* (2013).

Since the governing equations are solved in non-dimensional form using the normalizations $x_{ref} = H$, $u_{ref} = (\alpha g H \Delta T)^{1/2}$, $T_{ref} = \Delta T$ and $t_{ref} = x_{ref}/u_{ref}$, all results presented in the following are also non-dimensional, unless stated otherwise.

2.2. *Computational set-up*

The geometries used here to study turbulent RBC consist of a square cross-section in the x–z plane, i.e. $W_x = W_z$, and an aspect ratio satisfying $1/40 \leqslant \Gamma = W_y/W_z \leqslant 1$ in the y–z direction. A few examples of the instantaneous flow in different aspect-ratio containers are illustrated in figure 1. The confinement of the flow thus allows for a transition from a full 3-D to a quasi-2-D flow pattern. The Prandtl numbers Pr under investigation are 0.7 and 4.38, representing the properties of widely used media, namely air at ambient conditions and water at 40 °C. Table 1 summarizes the simulation parameters.

The meshes of all simulations are equidistant in the centre of the cell and gradually refined towards the walls, i.e. the grids are non-equidistant in all three coordinate

Pr	Ra	Γ	$N_x \times N_y \times N_z$	N_H	N_T	N_v	Nu_S	$Nu(\epsilon_T)$	$Nu(\epsilon_u)$	t_{avg}	
0.7	1×10^7	1	$162 \times 162 \times 162$	132	7/3.3	7/2.9	16.3	16.1	16.2	390	
0.7	1×10^7	1/4	$162 \times 50 \times 162$	132	7/2.8	6/2.4	16.0	16.3	16.4	100	
0.7	1×10^7	1/8	$162 \times 26 \times 162$	132	8/2.6	7/2.3	14.1	14.0	14.0	200	
0.7	1×10^8	1	$322 \times 322 \times 322$	281	7/3.9	6/3.4	31.3	31.1	31.6	400	
0.7	1×10^8	1/4	$322 \times 98 \times 322$	282	6/3.9	6/3.4	31.6	31.4	31.4	450	
0.7	1×10^8	1/8	$322 \times 50 \times 322$	285	8/4.0	8/3.5	33.8	34.0	34.1	480	
0.7	1×10^9	1/4	$722 \times 202 \times 722$	596	12/6.5	10/5.7	62.5	62.1	61.9	225	
0.7	1×10^9	1/8	$722 \times 114 \times 722$	596	11/6.6	10/5.8	63.4	63.0	63.0	425	
4.38	1×10^7	1	$178 \times 178 \times 194$	110	14/2.6	21/4.5	16.1	16.0	16.1	520	
4.38	1×10^7	1/2	$178 \times 90 \times 194$	110	14/2.7	21/4.4	15.9	15.9	15.9	250	
4.38	1×10^7	1/4	$178 \times 50 \times 194$	110	13/2.6	20/4.5	16.7	16.6	16.7	480	
4.38	1×10^7	1/8	$178 \times 26 \times 194$	110	15/2.7	22/4.6	14.9	14.9	14.8	380	
4.38	1×10^7	1/4	$178 \times 50 \times 194$	110	13/2.6	20/4.5	17.6	17.6	17.6	70	s.f. y-wall
4.38	1×10^7	1/8	$178 \times 26 \times 194$	110	15/2.7	22/4.6	19.7	19.7	19.7	100	s.f. y-wall
4.38	1×10^8	1	$258 \times 258 \times 258$	236	6/3.8	10/6.3	32.2	31.7	32.0	750	
4.38	1×10^8	1/2	$258 \times 136 \times 258$	236	6/3.7	10/6.2	31.8	31.6	31.8	240	
4.38	1×10^8	1/4	$258 \times 74 \times 258$	236	6/3.8	10/6.3	32.1	32.1	32.4	380	
4.38	1×10^8	1/8	$258 \times 40 \times 258$	236	6/3.9	9/6.5	35.0	34.3	34.6	370	
4.38	1×10^9	1	$514 \times 514 \times 514$	500	13/5.3	19/8.8	63.4	62.7	63.0	350	
4.38	1×10^9	1/2	$514 \times 276 \times 514$	500	13/5.3	19/8.8	63.2	63.2	61.7	239	
4.38	1×10^9	1/4	$514 \times 156 \times 514$	500	13/5.3	19/8.8	63.5	63.6	63.7	332	
4.38	1×10^9	1/8	$514 \times 98 \times 514$	508	13/5.5	18/9.1	67.8	67.8	67.7	230	
4.38	1×10^9	1/16	$514 \times 66 \times 514$	518	12/5.7	17/9.4	73.2	72.4	73.0	225	
4.38	1×10^9	1/32	$514 \times 34 \times 514$	500	13/5.3	19/8.8	61.7	61.4	61.1	120	
4.38	3×10^9	1	$770 \times 770 \times 770$	719	13/6.3	19/10.5	88.9	89.7	90.1	90	
4.38	3×10^9	1/4	$770 \times 220 \times 770$	719	13/6.3	19/10.5	89.2	88.5	88.8	184	
4.38	3×10^9	1/8	$770 \times 128 \times 770$	719	13/6.3	19/10.6	91.3	91.0	91.3	160	
4.38	3×10^9	1/16	$770 \times 82 \times 770$	719	12/6.6	18/11.0	100	99.5	99.6	315	
4.38	3×10^9	1/32	$770 \times 50 \times 770$	719	12/6.8	17/11.3	104	104.1	103.8	215	
4.38	1×10^{10}	1/4	$1142 \times 326 \times 1142$	1060	13/7.6	19/12.6	130.9	130.1	131.0	140	
4.38	1×10^{10}	1/8	$1142 \times 192 \times 1142$	1060	13/7.5	19/12.5	128.2	127.2	125.6	60	
4.38	1×10^{10}	1/16	$1142 \times 114 \times 1142$	1060	11/7.8	18/13.0	137.5	137.8	137.7	117	
4.38	1×10^{10}	1/32	$1142 \times 66 \times 1142$	1060	11/7.8	17/12.6	149.2	149.2	150.6	160	
4.38	1×10^{10}	1/40	$1142 \times 58 \times 1142$	1060	10/8.2	17/13.7	153.7	153.6	153.8	160	

TABLE 1. Simulation parameters and mean heat flux. Here, $N_x \times N_y \times N_z$ is the number of grid points in the respective spatial directions. The required number of grid points in the vertical direction is N_H and the numbers of grid points required to resolve the thermal and the viscous boundary layers are N_T and N_v repectively (actual resolution/requirement). The mean convective heat transfer is calculated through $Nu_S = \langle (RaPr)^{1/2} u_z T - \partial T/\partial z \rangle_S$, $Nu_{\epsilon_T} = (RaPr)^{1/2} \langle \epsilon_T \rangle_{global}$ and $Nu_{\epsilon_u} = (RaPr)^{1/2} \langle \epsilon_u \rangle_{global} + 1$. Here, t_{avg} denotes the averaging time of the simulations. Simulations performed with shear-free front and back walls at $y = 0$ and $y = W_y$ ($\partial u_x/\partial y = \partial u_z/\partial y = 0$) are denoted by 's.f. y-wall'.

directions. The meshes of all aspect ratios for one particular Ra and Pr are identical in the cross-section perpendicular to the y direction and are designed such that the resolutions of the boundary layers and in the middle of the y direction of the slender cells are approximately the same as for the cube. In particular, we designed the meshes such that the grid spacing in the centre of the cell is equidistant and smaller than the global estimate of the Kolmogorov and Batchelor length scales, and the

grid spacing becomes finer towards the side walls in order to sufficiently resolve the boundary layers, which has been illustrated in figure 2 of Kaczorowski & Xia (2013). The grid in the near-wall region is constructed with a hyperbolic tangent, where the wall spacing of the first grid point is chosen such that the grid point satisfies the resolution requirements for the boundary layer. This means that, depending on the Rayleigh number, the wall spacing of the first grid point is between 10^{-3} and 10^{-4} non-dimensional length. The achieved boundary-layer resolution can be found in table 1, from which one can see that our boundary-layer resolution is often two times as high as the requirement proposed by Shishkina *et al.* (2010). The resolution of the simulations exceeds the requirements proposed by Shishkina *et al.* (2010) not only in the boundary layers but also in the bulk. It has also been checked by examining local profiles through the centre of the cells that all relevant turbulent scales are sufficiently resolved (Kaczorowski & Xia 2013). Furthermore, the global Nusselt number is computed from a volume integration of the thermal and kinetic dissipation rates as, for instance, performed by Stevens, Verzicco & Lohse (2010). The results of this are provided in table 1. It can be seen from the table that there is no significant deviation between these values, indicating that the simulations are sufficiently resolved and averaged over a sufficiently long time to obtain an accurate prediction of the global Nusselt number. The averaging time is given in free-fall time units in table 1. Simulations were run for approximately 400 time units before we started averaging. For $Ra = 1 \times 10^8$, $Pr = 4.38$ and $\Gamma = 1$ we waited 800 time units before starting to average in order to test whether all transients have been dissipated.

3. Γ scaling of the flow

In the following section we analyse the influence of the aspect ratio on the local properties of the flow in the centre of the cell, which undergo a change from relatively homogeneous bulk turbulence to a boundary-layer-dominated flow. The influence on the local Bolgiano length scale and the dissipation rates is discussed in § 3.1, the velocity and temperature fluctuations and their probability density function are analysed in § 3.2 and the heat transfer through the centre of the cell is discussed in § 3.3.

3.1. *Analysis of the Bolgiano length scale*

We now discuss the influence of the lateral confinement on the local Bolgiano length scale defined (in terms of our non-dimensional variables) as

$$L_B(x, y, z) = \langle \epsilon_u(x, y, z)^{5/4} \rangle_t \langle \epsilon_T(x, y, z)^{-3/4} \rangle_t, \tag{3.1}$$

in order to investigate whether or not the smallest length of the confining geometry limits the extent of the Bolgiano length scale as suggested by Boffetta *et al.* (2012). Here, $\epsilon_T = (RaPr)^{-1/2} \sum_i (\partial T'/\partial x_i)^2$ is the non-dimensional temperature variance dissipation rate and $\epsilon_u = (Ra/Pr)^{-1/2} \sum_i \sum_j \left(\partial u_i'/\partial x_j\right)^2$ is the non-dimensional turbulent kinetic energy dissipation rate, and primed quantities denote turbulent fluctuations defined as $\phi = \bar{\phi} + \phi'$, so that the time average of ϕ' is $\bar{\phi'} = 0$. It follows by equating the second-order structure functions for K41 scaling,

$$\langle (\delta_r u)^2 \rangle_{V,t} = C \, \langle \epsilon_u \rangle_{V,T}^{2/3} \, r^{2/3}, \tag{3.2}$$

$$\langle (\delta_r T)^2 \rangle_{V,t} = C_T \, \langle \epsilon_T \rangle_{V,T} \, \langle \epsilon_u \rangle_{V,T}^{-2/6} \, r^{2/3}, \tag{3.3}$$

where C and C_T are the Kolmogorov constants for the respective structure functions, and the second-order structure functions for BO59 scaling,

$$\langle(\delta_r u)^2\rangle_{V,t} = C_{BO,u}\,\langle\epsilon_T\rangle_{V,T}^{2/5} r^{6/5}, \tag{3.4}$$

$$\langle(\delta_r T)^2\rangle_{V,t} = C_{BO,T}\langle\epsilon_T\rangle_{V,T}^{4/5} r^{2/5}, \tag{3.5}$$

where $C_{BO,u}$ and $C_{BO,T}$ are the respective proportionality factors, in the inertial range, that the mean Bolgiano length scale averaged over a certain subvolume V of the flow is given by

$$L_{B,V} = \langle\epsilon_u\rangle_{V,t}^{5/4}\langle\epsilon_T\rangle_{V,t}^{-3/4}. \tag{3.6}$$

Here, δ_r defines the increment of the velocity or temperature over a distance r, where r is either in the horizontal (x) or in the vertical (z) direction, depending on whether the longitudinal or transverse structure functions are to be analysed. In this paper the subvolume V is defined to be in the centre of the cell, the dimensions of which are 1/4 of the respective edge lengths W_x, W_y and W_z. We also averaged the dissipation rates over subvolumes in the centre of the cell with 1/2 and 1/8 of the cell's respective edge length and found that the scaling in all cases is the same, while the magnitude varies significantly for the 1/2-edge length volume, but results are almost identical for 1/4- and 1/8-edge length subvolumes. The global Bolgiano length scale can be written as

$$L_{B,global} = (Nu-1)^{5/4} Nu^{-3/4} (RaPr)^{-1/4}, \tag{3.7}$$

by averaging (3.6) over the entire volume and substituting the exact relations for the temperature variance dissipation rate $\langle\epsilon_T\rangle_V = Nu(RaPr)^{-1/2}$ and turbulent kinetic energy dissipation rate $\langle\epsilon_u\rangle_V = (Nu-1)(RaPr)^{-1/2}$ obtained from the Boussinesq equations into the equation (see also Lohse & Xia 2010).

The relationship between the lateral aspect ratio $\Gamma = W_y/W_z$ and the global Bolgiano length scale is presented in figure 2(*a*,*b*), illustrating that the globally averaged Bolgiano length scale does not change significantly with Γ. This can be explained through the relation $L_{B,global} \sim Nu^{1/2}$, which for constant Ra and Pr yields a Γ variation of $L_{B,global}$ of approximately 1 %, since the maximum variation of Nu with Γ is approximately 10 % (cf. table 1). The local Bolgiano length scale in the core region shown in figure 2(*c*,*d*), on the other hand, is significantly influenced by Γ. It is observed that $L_{B,centre}$ decreases as Γ decreases and that the rate at which $L_{B,centre}$ decreases is larger for $Pr = 0.7$ than for $Pr = 4.38$ (note the difference in the horizontal axis scales between figures 2*c* and 2*d*). We observe that the local Bolgiano length scale in the centre of the box is smaller than the width of the cell for sufficiently large Γ. For our largest Ra and small Γ with $Pr = 4.38$, it is found that both $L_{B,centre}$ and $L_{B,global}$ are larger than W_y, while Boffetta *et al.* (2012) state that the local Bolgiano length scale in their simulations is always smaller than the smallest length of the geometry. Therefore, although the smallest dimension of the cell does not limit the global Bolgiano length scale, it does limit the local Bolgiano length scale $L_{B,center}$ in the sense that $L_{B,center}$ is now of the same order of magnitude as the smallest cell dimension and its decrease approximately follows the decrease of the smallest cell dimension. We conclude that confinement of the flow reduces the local Bolgiano length scale, which then can be used to study the impact on the structure function scaling at high Ra, when the local $L_{B,centre}$ in a cube would be very large and therefore would not allow for the observation of a cross-over from

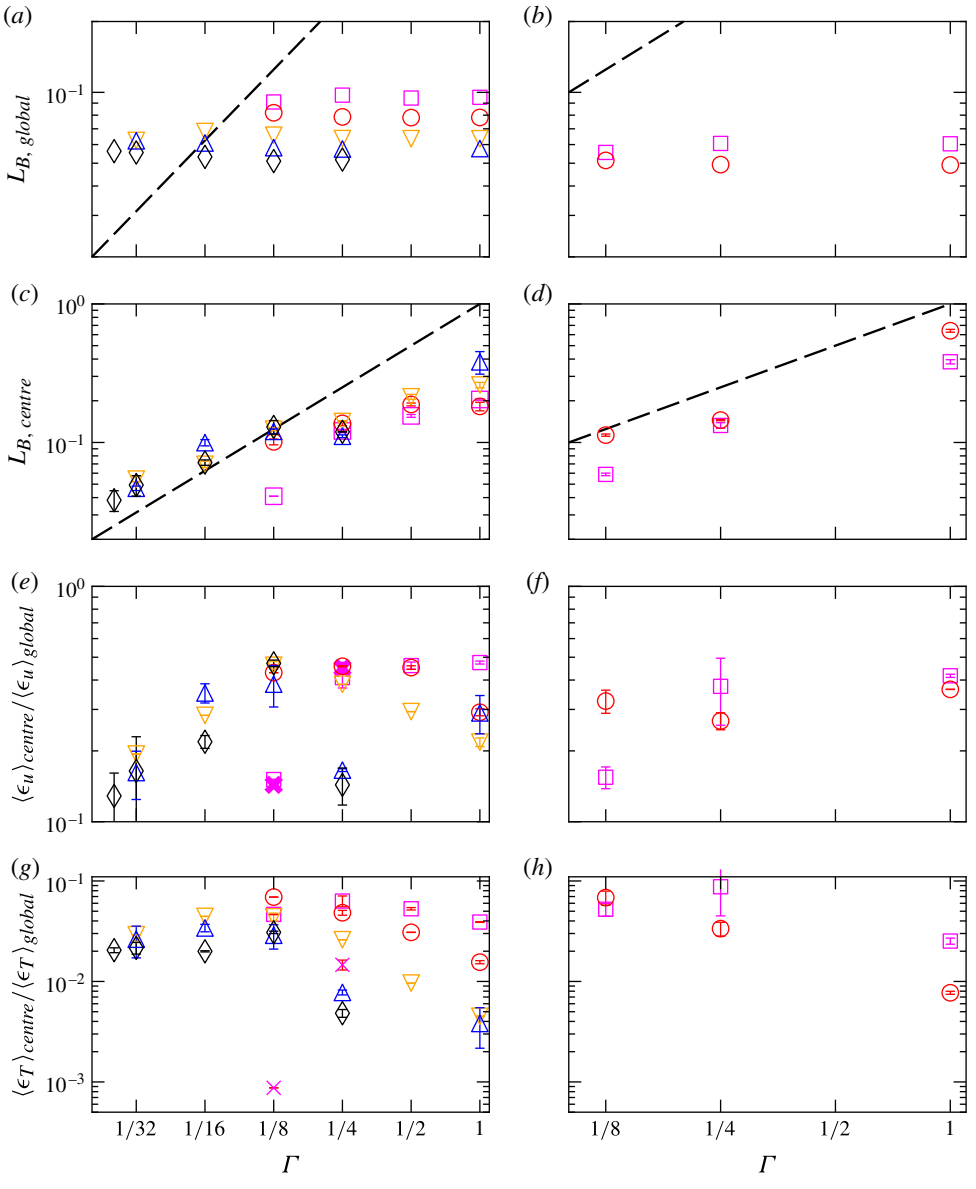

FIGURE 2. (Colour online) The Γ dependence of the global Bolgiano length scale (*a*,*b*), the local Bolgiano length scale (*c*,*d*), where the black dashed line represents the scaling when the lateral extent of the convection cell equals the Bolgiano length scale, i.e. $L_B = W_y$, (*e*,*f*) the Γ dependence of the turbulent kinetic energy dissipation rate locally averaged in the centre of the cell normalized with the globally averaged value and (*g*,*h*) the Γ dependence of the temperature variance dissipation rate locally averaged in the centre of the cell normalized with its globally averaged value. The dependence for $Pr = 4.38$ is shown in (*a*), (*c*), (*e*) and (*g*) and the dependence for $Pr = 0.7$ in (*b*), (*d*), (*f*) and (*h*). Here, $Ra = 1 \times 10^7$ (□), $Ra = 1 \times 10^7$ with $\partial v/\partial y|_{wall} = 0$ (×), $Ra = 1 \times 10^8$ (○), $Ra = 1 \times 10^9$ (▽), $Ra = 3 \times 10^9$ (△) and $Ra = 1 \times 10^{10}$ (◇). Note that $L_B = 1$ corresponds to the cell height $H = W_z$.

K41 to BO59 scaling in RBC. In figure 2 (and in subsequent figures), the error bars represent the differences between the time-averaged quantities using the full time series and only half of the time series.

In Huang *et al.* (2013) the impact of lateral confinement on the large-scale flow and the global heat transport was highlighted. It is therefore interesting to take a closer look in order to gain a deeper understanding of the dynamics of the bulk. Here, we focus primarily on the properties of the flow in the core region, in particular the Γ dependence of the turbulent kinetic energy dissipation rate ϵ_u and the temperature variance dissipation rate ϵ_T. From figure 2(*e*,*g*) it becomes clear that both $\langle\epsilon_u\rangle_{centre}/\langle\epsilon_u\rangle_{global}$ and $\langle\epsilon_T\rangle_{centre}/\langle\epsilon_T\rangle_{global}$ exhibit a maximum at a certain Γ that is a function of Ra. With increasing Ra this maximum is shifted towards smaller Γ.

In order to examine the effect of the viscous drag of the lateral sidewalls (in the y direction), we conducted simulations for $Ra = 1 \times 10^7$, $Pr = 4.38$ and aspect ratios of $\Gamma = 1/8$ and $\Gamma = 1/4$ with free-slip lateral (y) walls, while a no-slip condition was still imposed on all other walls and the temperature boundary conditions were unchanged. A significant change of the global Nusselt number (Nu is approximately 30 % higher with the free-slip condition) is also observed for $\Gamma = 1/8$, while only a 7 % increase of Nu is found for $\Gamma = 1/4$, showing that the effect of the sidewalls for $\Gamma = 1/4$ is relatively small, but still significant. It is interesting to note that removal of the no-slip condition on the y-walls has a significant impact on the temperature variance dissipation rate in the centre of the cell, which becomes significantly smaller than in the case with viscous y-walls. The normalized turbulent kinetic energy dissipation rates, however, are nearly unaffected by changing the velocity boundary conditions on the sidewalls. The influence of the lateral viscous boundary layers on the flow and the impact of confinement on the heat transfer should be an interesting field for further study, to unravel the key elements that lead to confinement-induced heat transfer enhancement. Here, we just wish to point out that the effective width of the cell, which is determined by the thickness of the boundary layers on the sidewall, plays a key role in the heat transfer enhancement mechanism. This can be seen from the comparison of the no-slip and free-slip cases in table 1. While for $Ra = 1 \times 10^7$ $\Gamma = 1/4$ is close to the optimum Γ (in terms of heat transfer) and smaller Γ lead to a sharp drop in Nu, the effective width of the shear-free cell is still too large to result in a drop of Nu. Analysis of the boundary layer thicknesses on the y-walls discussed in § 3.3 reveals the importance of the cell width compared to the sidewall boundary-layer thickness. This phenomenon will be studied in detail in a subsequent publication.

Furthermore, figure 2(*e*,*f*) highlights that the resolution requirement for the core region becomes increasingly more demanding as Γ is reduced towards roughly twice the boundary-layer thickness, since the local dissipation rates increase significantly for high Ra. It is, however, noted that both ϵ_u and ϵ_T decrease again for even smaller Γ. We know from Huang *et al.* (2013) that this is related to the fact that the thermal plumes become more coherent and are more likely to travel vertically through the bulk as the aspect ratio is reduced. We find that the resolution in these cases is $\eta_b/\Delta x_p \approx 1.1 \ldots 1.2$, showing that the mean field is still well resolved. It is, however, reckoned that the thermal plumes and their associated strong gradients are not sufficiently resolved, which might in turn result in an erroneous dissipation rate. The effect of under-resolving the bulk is further discussed in § 5.

The different dynamics of the large-scale flow for the different aspect-ratio geometries are illustrated for the plane $y = W_y/2$ in figure 3. They show that the flow is sufficiently stable for large aspect ratios, since an LSC can be clearly identified from the time-averaged velocity field. Hence, the core region is stirred by the LSC,

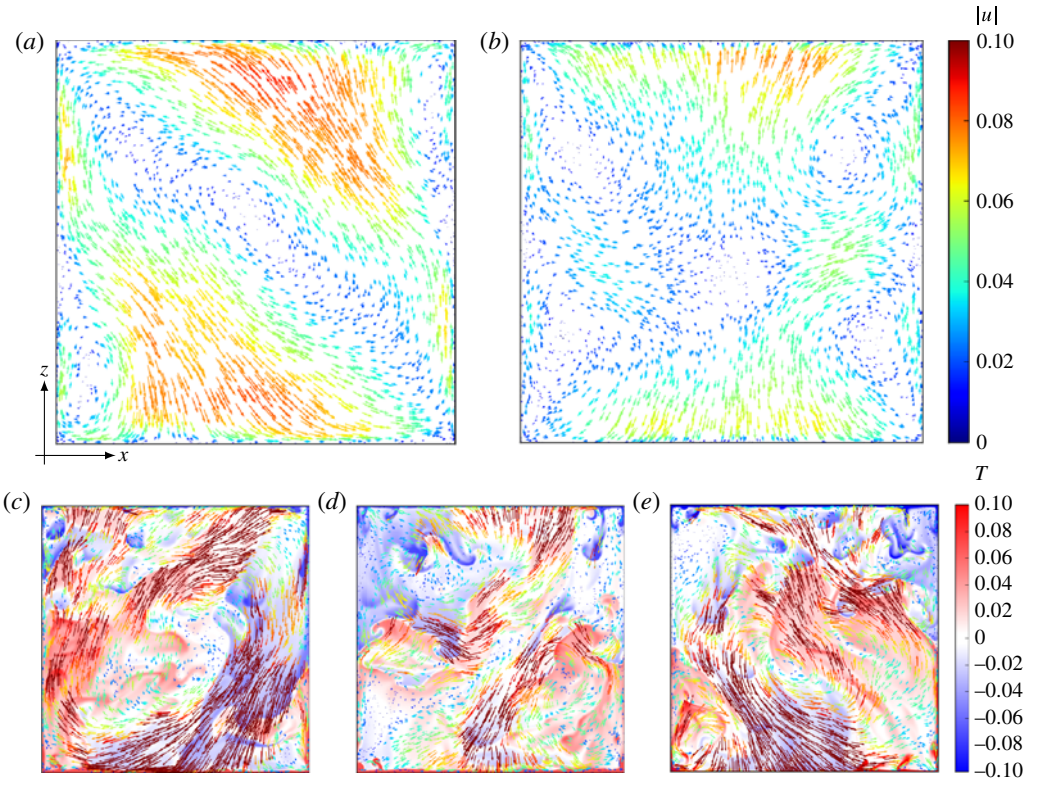

FIGURE 3. (Colour online) Mean in-plane normalized velocity vectors coloured by their magnitude in the centre plane $y = W_y/2$ for (*a*) $\Gamma = 1/4$ and (*b*) $\Gamma = 1/8$ for $Ra = 1 \times 10^9$ and $Pr = 4.38$. (*c*)–(*e*) The instantaneous flow in the $\Gamma = 1/8$ geometry underlying the mean field in (*b*). The three snapshots are for times $t = 400$, 450 and 485 with the velocity vectors coloured according to the colour scale in (*a*,*b*) and the temperature field coloured from blue (cold) to red (hot).

as can be seen from figure 3(*a*). For $\Gamma = 1/8$, however, this is not the case, as can be seen from 3(*b*). The LSC has become unstable with frequent reversals of the LSC direction, which is illustrated in figure 3(*c*–*e*). The series of instantaneous snapshots provides an example of such a reversal, where plumes frequently propagate through the centre region of the flow. The frequent reversals of the LSC and its breakdowns can be more clearly observed from the complementary movie. Based on short-time averages of their experimental data, Sun, Xia & Tong (2005*b*) showed that averaging of two mean fields with opposite sense of flow direction yields a four-roll pattern similar to the one illustrated in figure 3(*b*).

3.2. *Analysis of turbulent fluctuations*

The influence of the aspect ratio on the flow is also reflected by the increased turbulent fluctuations in the bulk region in terms of the Reynolds number $(Re) = (Ra/Pr)^{1/2} w_{rms} H$, with $w_{rms} = (\langle (w')^2 \rangle)^{1/2}$. The Γ dependence of the velocity fluctuations represented by $Re_{rms}(\Gamma)$ presented in figure 4(*a*,*b*) exhibits a clear maximum for the highest Ra, while our data set does not comprise small enough

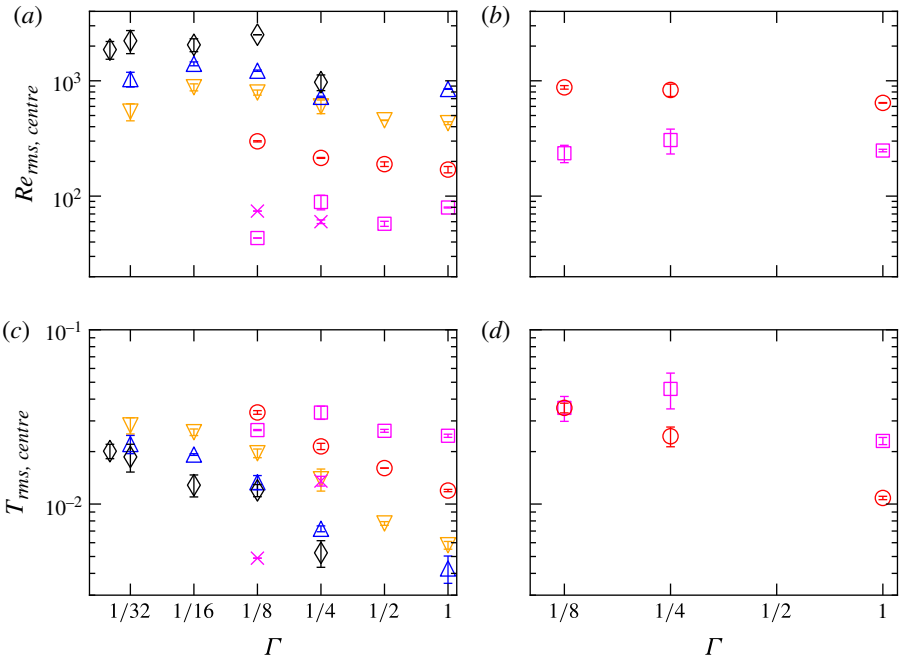

FIGURE 4. (Colour online) The Γ dependence of the turbulent fluctuations $Re = (Ra/Pr)^{1/2} w_{rms} H$ and $T_{rms} = (\langle (T')^2 \rangle)^{1/2}$ averaged in time and the centre volume $V_{centre} = \Gamma 0.25^3$ for $Pr = 4.38$ (*a*,*c*) and $Pr = 0.7$ (*b*,*d*): $Ra = 1 \times 10^7$ (□), $Ra = 1 \times 10^7$ with free-slip *y*-walls (×), $Ra = 1 \times 10^8$ (○), $Ra = 1 \times 10^9$ (▽), $Ra = 3 \times 10^9$ (△) and $Ra = 1 \times 10^{10}$ (◇).

Γ for $Ra \leqslant 1 \times 10^8$ to observe the maximum. Analysis of the Γ dependence of the turbulent temperature fluctuations $T_{rms} = (\langle (T')^2 \rangle)^{1/2}$ presented in figure 4(*c*,*d*) shows that the fluctuations increase with decreasing aspect ratio. A maximum as observed for the velocity fluctuations is not observed, although the shape of $T_{rms}(\Gamma)$ suggests that there might be one for very small Γ.

The different dynamics of the bulk flow may also be presented by plotting the bulk fluctuations as a function of *Ra* (figure 5). Although the plot is a little scattered, the plot highlights the impact of the aspect ratio on the magnitude of the fluctuations, which reflects the different dynamics of the flow presented in figure 3. While for very small aspect ratios the flow constantly undergoes reversals, it is relatively stable for large aspect ratios, which will affect the mean velocity profile. However, we note that the mean value in the centre of the cell is very small (smaller than 0.01 for $Ra = 1 \times 10^9$) for all aspect ratios. We therefore conclude that the different magnitude of the fluctuations in the centre represents a feature of the flow.

We therefore investigate the p.d.f.s of the vertical velocity and the temperature fluctuations in the bulk and observe that the aspect ratio has a significant impact on the shape of the p.d.f.s. The p.d.f. of the vertical velocity fluctuations plotted in figure 6(*a*) is essentially Gaussian for $\Gamma = 1/8$, while the p.d.f.s of the vertical velocity fluctuations for larger Γ show a significant deviation from the Gaussian distribution. The deviation from the Gaussian distribution is, however, not as high as for the temperature fluctuations, which are presented in figure 6(*b*). For $\Gamma = 1/8$ a Gaussian-like p.d.f. is observed, while the p.d.f. for $\Gamma = 1$ exhibits a very large kurtosis. From this it could be inferred that the bulk flow in the small-aspect-ratio

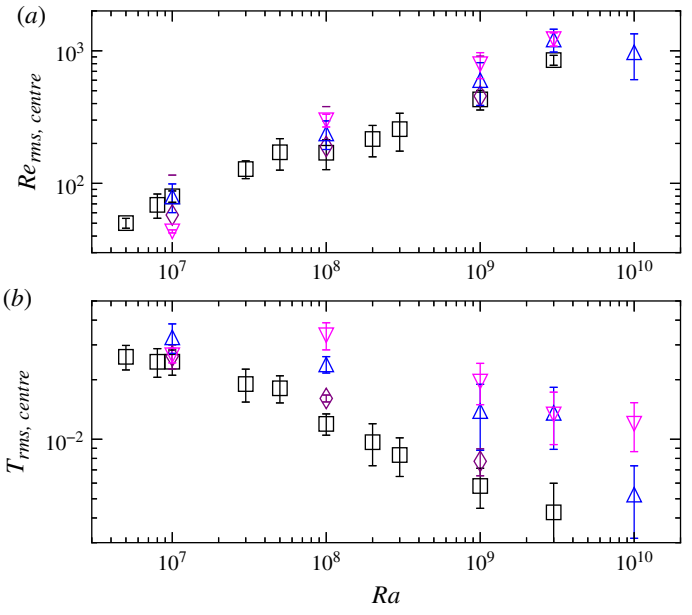

FIGURE 5. (Colour online) The Ra dependence of the turbulent fluctuations averaged in time and the centre volume $V_{centre} = \Gamma 0.25^3$ for $Pr = 4.38$. Here, $\Gamma = 1$ (□), $\Gamma = 1/2$ (◇), $\Gamma = 1/4$ (△) and $\Gamma = 1/8$ (▽).

cells is well mixed; however, it has to be taken into account that T_{rms} is significantly larger for small Γ, which is also evident from the online supplementary movie available at http://dx.doi.org/10.1017/jfm.2014.154. In this context we would also like to refer to Huang *et al.* (2013), where it was already observed that the thermal plumes become larger and more coherent as the aspect ratio is reduced.

The scale dependences of the p.d.f.s of the fluctuations with spatial separations r in the inertial range are presented in figure 7 for $\Gamma = 1/2$ and $\Gamma = 1/8$. It is revealed that for both aspect ratios the temperature field in the bulk is more intermittent than the velocity field, since the shape of the p.d.f.s changes significantly more. Zhou & Xia (2010) observed exponential tails of $P(\delta_r w'/(\delta_r w')_{rms})$ for r at the integral scale in a cylindrical cell of aspect ratio unity filled with water. In our simulations we observe a similar tendency, but the trend is not as clear as in the experimental observations.

Comparison of the aspect-ratio dependence of the velocity and temperature fluctuations obtained from our simulations indicates that the dynamics of the temperature field is much more sensitive to changes of the aspect ratio than the velocity fluctuations. The relatively thick viscous laminar boundary layers adjacent to the lateral walls seem to dampen the fluctuations in the bulk, which we will investigate in the following section.

3.3. *Influence of the sidewalls on the bulk flow*

Since we are going to compare the heat flux through the centre of the cell in § 4, we will analyse the profiles of the vertical convective heat flux $Nu_c = \langle wT'\sqrt{RaPr}\rangle_{x,z}$ averaged over 2-D regions with $3/8 \leqslant x, z \leqslant 5/8$. In figure 8 the profiles of the mean heat flux are plotted as a function of the lateral coordinate y. It is revealed

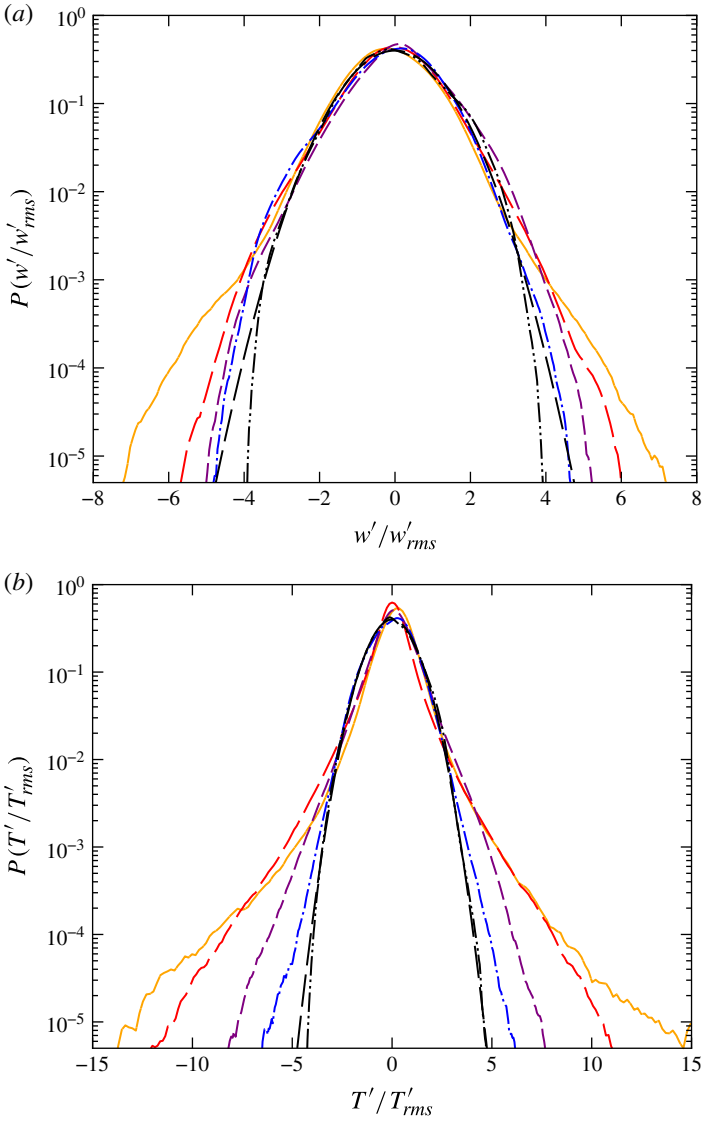

FIGURE 6. (Colour online) The p.d.f.s of (*a*) the vertical velocity fluctuation w_{rms} and (*b*) the temperature fluctuation T_{rms} in the core region ($V_{centre} = \Gamma 0.25^3$) for aspect ratios $\Gamma = 1/16$ (–··–), $1/8$ (–·–), $1/4$ (– –), $1/2$ (— —) and 1 (—) with $Ra = 1 \times 10^9$ and $Pr = 4.38$. A Gaussian distribution (– –) with the same standard deviation as the respective distributions for $\Gamma = 1/16$ is given for reference.

that the distribution of the heat flux in the lateral direction is strongly dependent on the aspect ratio Γ. The local heat flux is largest close to the lateral sidewalls and very small in the centre of the cell. However, with decreasing aspect ratio the centre region vanishes and the regions that are influenced by the lateral boundary layers begin to overlap, so that for $\Gamma = 1/8$ the heat flux in the centre of the cubic cell becomes largest. The aspect-ratio dependence of the distribution of the local heat flux is therefore significantly different from the distribution in the centre plane $y/W_y = 0.5$

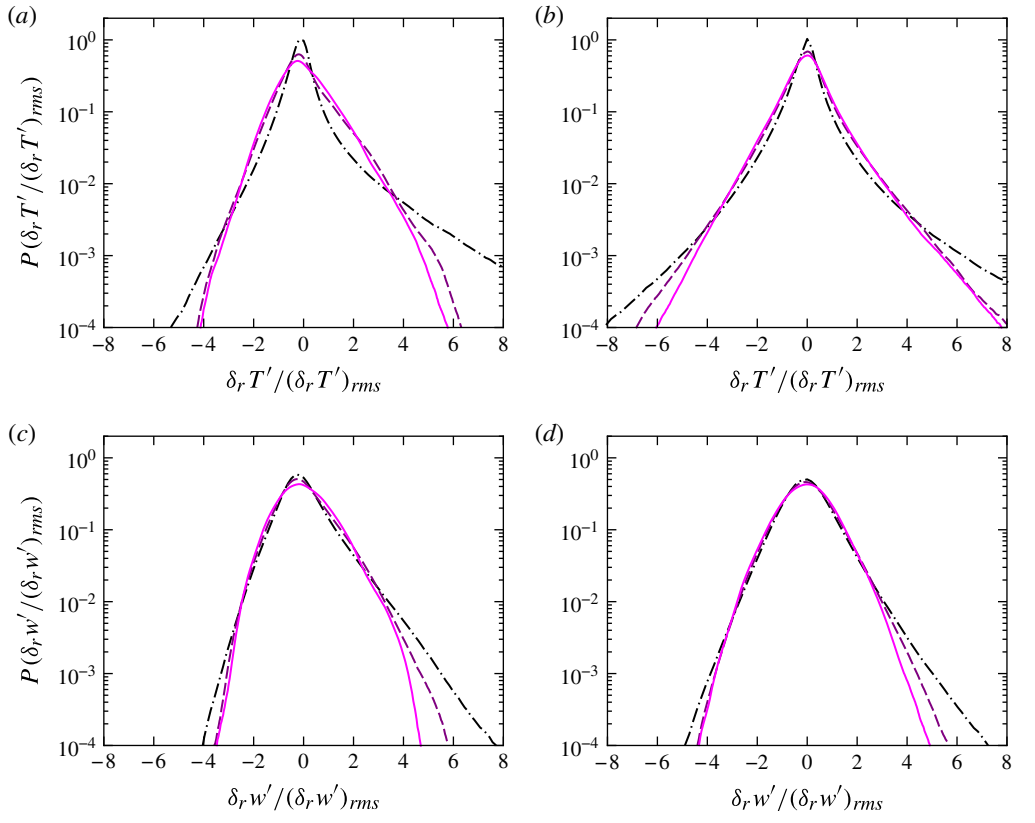

FIGURE 7. (Colour online) The p.d.f.s of the increments of the temperature fluctuations (*a*,*b*) and of the vertical velocity fluctuations (*c*,*d*) with different separations r for $Ra = 1 \times 10^9$, $Pr = 4.38$ with $\Gamma = 1/8$ (*a*,*c*) and $\Gamma = 1/2$ (*b*,*d*) in the core region ($V_{centre} = \Gamma 0.25^3$) of the cell. Here, $r \approx \eta_k$ (– · –), $r \approx 10\eta_k$ (– –) and $r \approx 0.40H$ (—).

as observed in Huang *et al.* (2013), where it was observed that the heat flux increases not only close to the sidewalls of the square cross-section (x–z plane), but also in the centre, as the aspect ratio is reduced from $\Gamma = 1/2$ to $1/8$. Together with the present analysis it becomes clear that the increase of the heat flux in the centre is due to the influence of the lateral sidewalls. Although the impact of periodic boundaries on the bulk dynamics would also be interesting to study, we are presently mainly concerned with highly confined flow, and therefore we do not consider periodic boundaries here. From figure 8(*a*,*c*) it can also be seen that even a shear-free lateral wall still exhibits some sort of near-wall region with a significantly higher heat flux than the bulk. It is, however, interesting to note that the heat flux in the lateral direction through the centre of the cell is generally smaller than with viscous lateral walls, indicating that in this case more heat is carried by the LSC and less through the bulk. In other words, the friction of the sidewalls destabilizes the LSC and leads to larger heat transport through the bulk.

Since the boundary layers on the y-walls have a significant impact on the dynamics of the system, we wish to analyse the thickness relative to the cell width W_y. Here, we define the boundary layers on the y-walls by the root-mean-square (r.m.s.) values of the wall-normal temperature and velocity profiles (Xin & Xia 1997; Qiu & Xia

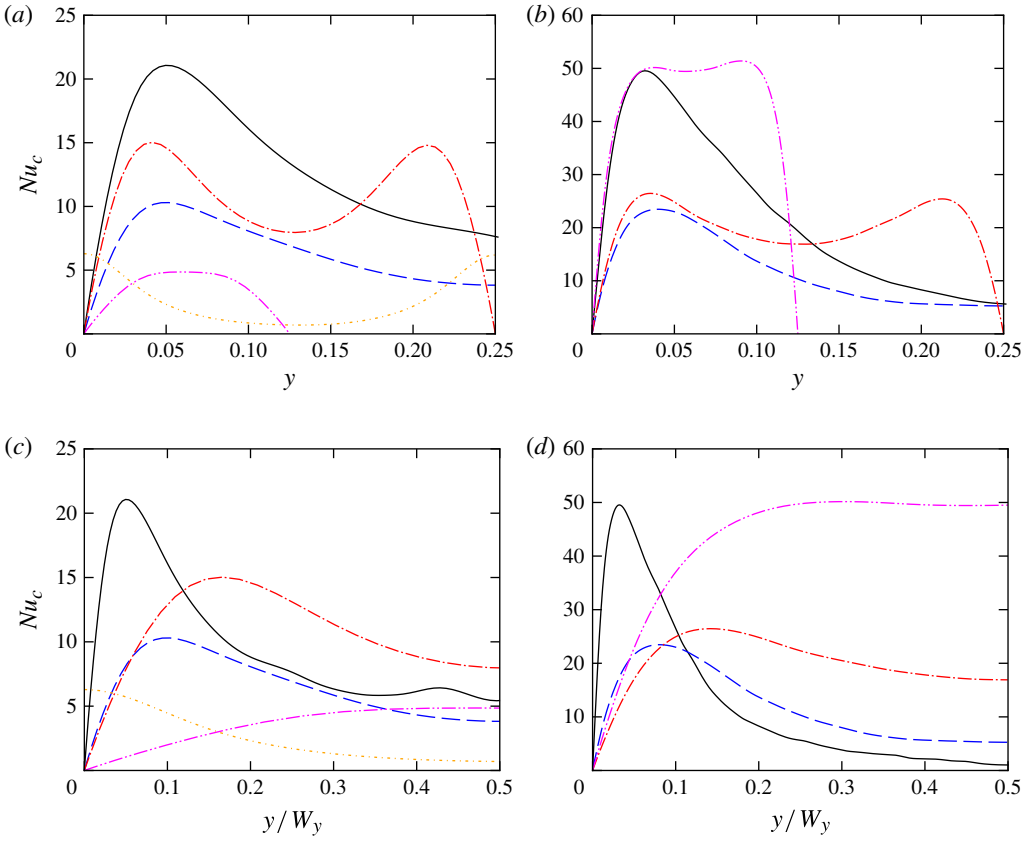

FIGURE 8. (Colour online) Profiles of the vertical convective heat flux averaged over the 2-D region $(3/8 \leqslant x, z \leqslant 5/8)$ as a function of the lateral coordinate y (a,b) and the normalized lateral coordinate y/W_y (c,d) for $Ra = 1 \times 10^7$ (a,c) and $Ra = 1 \times 10^9$ (b,d). Here, $\Gamma = 1/8$ (–··–), $\Gamma = 1/4$ (–·–), $\Gamma = 1/2$ (– –) and $\Gamma = 1$ (—) with $Pr = 4.38$. The dot-dashed curve in (a,c) is a $\Gamma = 1/4$ cell with shear-free lateral walls.

1998), as illustrated in figure 9. While the velocity boundary layer is defined by the maximum of the vertical velocity fluctuations (see figure 9*a*), the thermal boundary layer is defined as the intersection of the tangent through the maximum of the profile $(\partial T/\partial y = 0)$ and the secant through the logarithmic r.m.s. temperature profile at $y_1 = 0.05$ and $y_2 = 0.1$. The thermal boundary-layer thickness is therefore given by $\delta_{\sigma_T} = \exp(\log(y_1) + (T_{rms}(y = 0) - T_{rms}(y_1))/b)$, where $b = (T_{rms}(y_2) - T_{rms}(y_1))/(\log(y_2) - \log(y_1))$. While the boundary layers have already merged for $\Gamma = 1/8$ and $Ra = 1 \times 10^8$, the profile of the r.m.s. values of T still shows two separate peaks for $Ra = 1 \times 10^9$. However, the abovementioned method fails in this case, since the boundary layers have almost merged, so that no sufficiently large region exists to define the secant. Here, we use the peaks of the profile as the boundary-layer thickness. For $\Gamma < 1/8$ the thermal boundary layers have merged, so that only one peak in the centre of the cell exists. This so-defined thermal boundary layer might be understood as the near-wall region that is affected by the thermal plumes that predominantly flow along the vertical walls. The results of this analysis are plotted in figure 10. The figure demonstrates that the sidewall boundary layers merge when

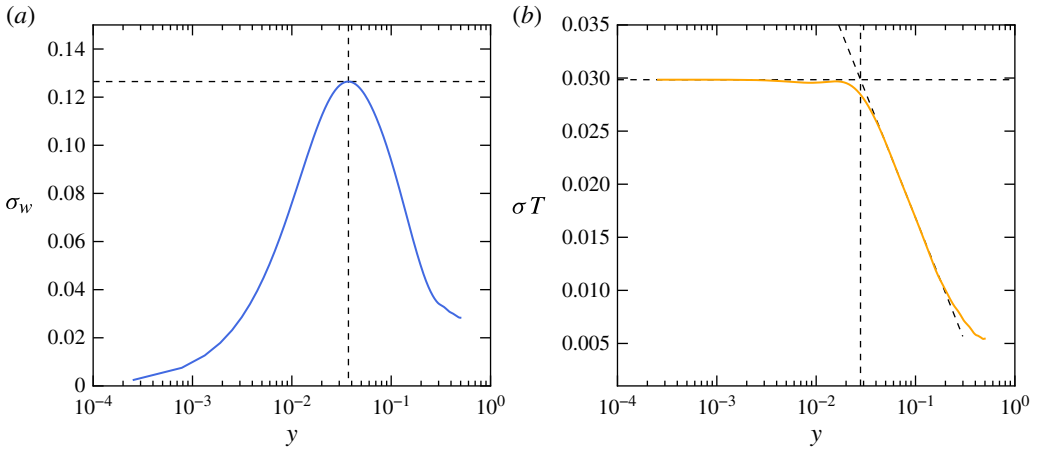

FIGURE 9. (Colour online) Illustration of the definition of the viscous-boundary-layer thickness (*a*) and the thermal-boundary-layer thickness (*b*) adjacent to the *y*-walls. The profiles are taken from the case $Ra = 1 \times 10^9$, $Pr = 4.38$ and $\Gamma = 1$.

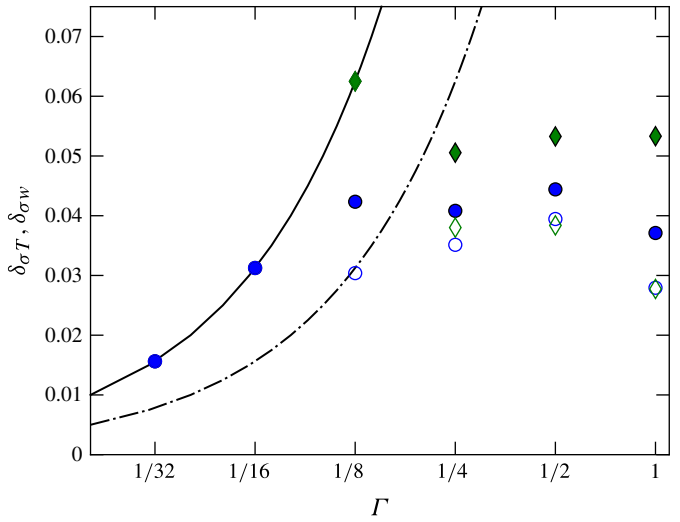

FIGURE 10. (Colour online) The Γ dependence of the thermal- and viscous-boundary-layer thicknesses on the lateral walls averaged over the 2-D region $(3/8 \leqslant x, z \leqslant 5/8)$ for $Pr = 4.38$: $Ra = 1 \times 10^8$ (δ_{σ_w} ♦; δ_{σ_T} ◇), $Ra = 1 \times 10^9$ (δ_{σ_w} ●; δ_{σ_T} ○). The viscous-boundary-layer thickness is defined by the maximum r.m.s. value of the vertical velocity normal to the wall and the thermal-boundary-layer thickness is determined by the distance. Any point that lies above the dot-dashed curve indicates that the averaging volume used to evaluate the centre of the flow also contains (at least partially) contributions from the sidewall boundary layers. The solid curve represents the half-cell width.

Γ falls below a certain value that is dependent on Ra, which is when the global Nusselt number exhibits its maximum. The figure also illustrates the extension of the averaging volume in the centre of the cell, indicated by the dot-dashed curve. If the boundary-layer thickness is above this line in figure 10, the analysis of the

centre region will contain contributions from the boundary layers. The illustration of the r.m.s. velocity profile in figure 9(*a*) indicates that due to entrainment the centre region is even affected when the boundary-layer thickness is slightly smaller than indicated by the dot-dashed curve. Entrainment and interactions between the boundary layers on the sidewalls might also explain why there is a sudden increase of the boundary-layer thickness when the boundary layers from the two opposite walls merge for $Ra = 1 \times 10^8$. Strictly speaking, in these cases the centre of the cell cannot be considered as bulk flow in the usual sense. However, one might take the view that lateral confinement changes the flow to a boundary-layer-dominated flow.

4. Energy balance

As in Kaczorowski & Xia (2013), we compute the local heat flux

$$Nu_{centre} \equiv (RaPr)^{1/2} \langle wT' \rangle_{t,centre} \tag{4.1}$$

in the core region of the flow, where w is the vertical velocity and T' is the fluctuating component of the temperature, and compare it with its estimate based on the turbulent kinetic energy dissipation rate $\epsilon_u = (Ra/Pr)^{-1/2} \sum_i \sum_j \left(\partial u_i/\partial x_j\right)$,

$$Nu_{centre} = \langle \epsilon_u \rangle_{centre} (RaPr)^{1/2}, \tag{4.2}$$

which was shown to hold in the bulk of cylindrical geometries filled with water (Shang *et al.* 2004; Ni *et al.* 2011), while the estimate based on the temperature variance dissipation rate $\epsilon_T = (RaPr)^{-1/2} \sum_i (\partial T/\partial x_i)$,

$$Nu_{centre} = \langle \epsilon_T \rangle_{centre} (RaPr)^{1/2}, \tag{4.3}$$

was found not to hold in a cylindrical geometry filled with water (Shang *et al.* 2008). We observed previously (Kaczorowski & Xia 2013) that for a cubic geometry with $Pr = 0.7$ none of the above estimates match the directly measured heat flux, and even for the water case ($Pr = 4.38$) we observed a good agreement of (4.1) and (4.2) only for low Ra. A significant difference between a cubic and a cylindrical geometry is the orientation of the LSC in the two geometries. While it is aligned with one of the diagonal directions in the cube, it is randomly oriented and less stable in a cylinder. We therefore now compare the quantities (4.1)–(4.3) for Cartesian geometries of varying aspect ratio, where it is known that the LSC is more unstable at low aspect ratios. Hence, we intend to investigate the influence of the plumes on the abovementioned relationships.

From figure 11 it can be concluded that the decreasing aspect ratio not only increases the heat transfer through the core region, but also leads to a better balance between the heat transfer and the dissipation of turbulent kinetic energy. It can also be seen that in the small-aspect-ratio cases this energy balance also holds for the cases with $Pr = 0.7$, while it was previously observed (Kaczorowski & Xia 2013) that the directly measured Nu lies between the estimates from the turbulent kinetic energy dissipation rates and the temperature variance dissipation rates. This might be a result of the different flow topologies, as discussed in § 3.1 and illustrated in figure 3. While a stable LSC exists for high Ra in the $\Gamma = 1$ cell, the LSC becomes more and more unstable as the flow is more confined, hence resulting in more vertical flow through the core region. This in turn implies that a balance of the local heat flux and the dissipation of turbulent kinetic energy is only given when a sufficient

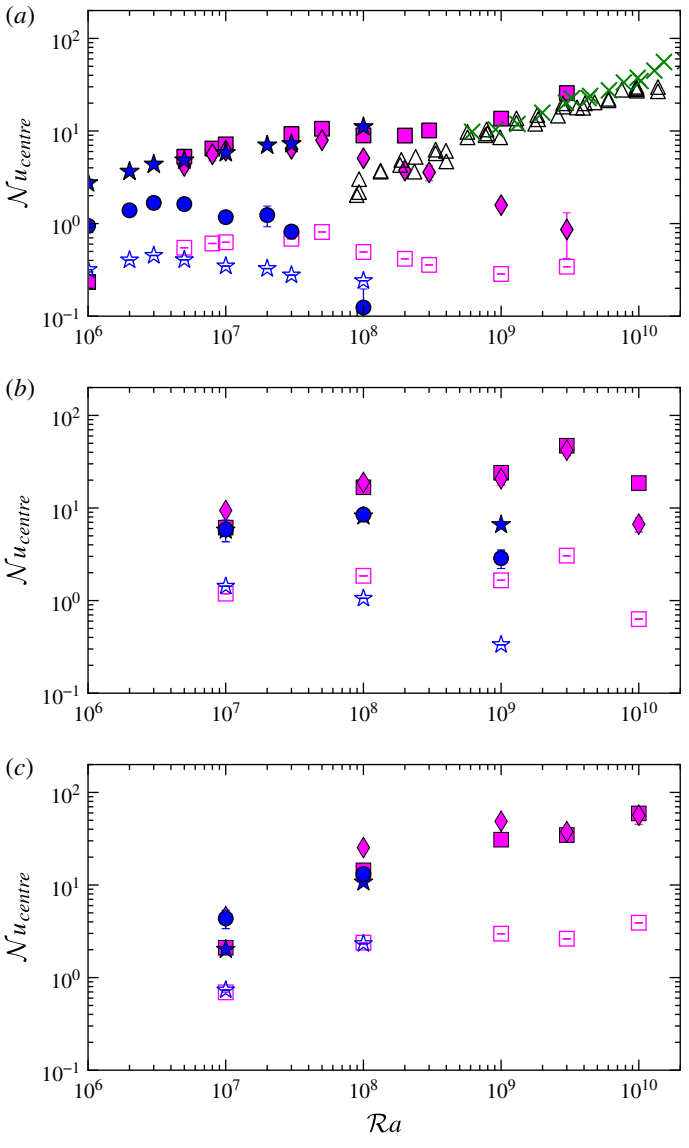

FIGURE 11. (Colour online) The Ra scaling of the local vertical heat transfer for (a) the cube (results taken from Kaczorowski & Xia (2013)), (b) the aspect ratio $\Gamma = 1/4$ and (c) the aspect ratio $\Gamma = 1/8$ cell. Direct measurements of the local vertical heat transfer ($Pr = 0.7$: ●; $Pr = 4.38$: ♦), the local Nusselt number calculated through (4.2) ($Pr = 0.7$: ♦; $Pr = 4.38$: ■) and (4.3) ($Pr = 0.7$: ■; $Pr = 4.38$: □) in the centre region with the volume $V_{centre} = \Gamma 0.25^3$. In ($a$) the data are compared with experimental data for direct measurements of Nu (△) (Shang, Tong & Xia 2008) and Nu calculated from the turbulent kinetic energy dissipation rates (×) (Ni *et al.* 2011), both measured in the centre of cylindrical cells.

number of plumes are involved. This is the case when the aspect ratio is reduced and the LSC becomes more unstable, so that the scaling of the low-aspect-ratio cells approaches the scaling obtained in the cylindrical cells.

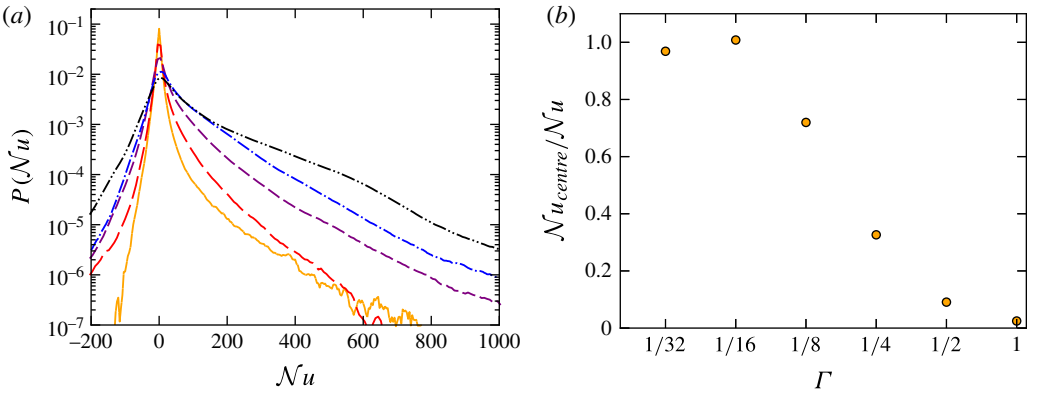

FIGURE 12. (Colour online) (*a*) The p.d.f.s of the vertical convective heat flux Nu in the core region ($V_{centre} = \Gamma 0.25^3$) for aspect ratios $\Gamma = 1/16$ (–··–), $1/8$ (–·–), $1/4$ (- - -), $1/2$ (– –) and 1 (—) with $Ra = 1 \times 10^9$ and $Pr = 4.38$. (*b*) The Γ dependence of the vertical convective heat flux Nu_{centre} (●) in the core region ($V_{centre} = \Gamma 0.25^3$) normalized with the globally averaged heat flux Nu for $Ra = 1 \times 10^9$ and $Pr = 4.38$.

For a more detailed analysis we compare the p.d.f.s of the vertical convective heat flux through the core region of cells with different aspect ratios calculated from (4.1) in figure 12(*a*). All geometries have in common that the most probable heat flux in the centre of the cell is zero and the p.d.f.s are positively skewed with almost exponential left tails and intermittent right tails. However, it can also be seen that the probability of extreme events increases with decreasing aspect ratio in the lateral direction. In particular, the right tail becomes strongly intermittent for small aspect ratios, which is probably linked to the increasingly unstable LSC and eventually results in a higher mean heat transfer through the core region at lower aspect ratios.

This is also reflected by a direct comparison of the local heat flux through the centre of the cell Nu_{centre} and the globally averaged heat flux that is reported in table 1, as presented in figure 12(*b*). It becomes clear that in the cube for $Ra = 1 \times 10^9$ and $Pr = 4.38$ only a negligible amount of heat is transported through the centre of the cell, while the centre of the cell contributes approximately three-quarters to the global heat transfer when $\Gamma = 1/8$. For aspect ratios $\Gamma \leqslant 1/16$ the vertical convective heat flux in the centre is as large as the global heat flux.

4.1. *Energy flux*

One of the very few exact relations in turbulence study is Kolmogorov's four-fifths law, which is derived under the condition of local isotropy. A generalized version of the law, which is local in both space and time, was later obtained without requiring the flow to be strictly locally isotropic but by spherically averaging the structure function over all directions (Duchon & Robert 2000; Eyink 2003), i.e.

$$\epsilon_{centre}(r, t) = \frac{\langle (\delta_r u_r(r, t))^3 \rangle_{centre}}{-4/5r}, \tag{4.4}$$

where the structure function is averaged in all directions. This instantaneous local dissipation rate may also be interpreted as an energy flux, defined positive when it flows from large to small scales. Although $\epsilon_{centre}(r, t)$ is on average positive, its

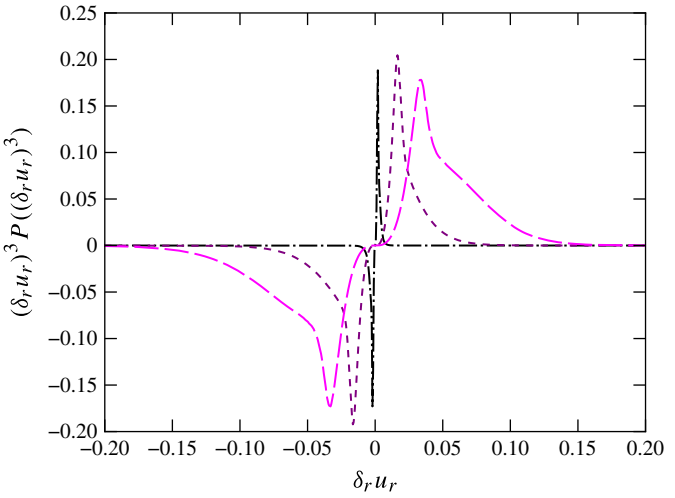

FIGURE 13. (Colour online) The integral kernel of the third-order structure function evaluated in the centre of the cell for $Ra = 1 \times 10^9$, $Pr = 4.38$ and $\Gamma = 1$. The different curves represent the spatial separation r in the dissipative range (—), (close to) the inertial range (- -) and at large scale (– –) indicated by the symbols in figure 14.

fluctuating sign shows that energy cascade can momentarily reverse its direction, i.e. from small to large scales in what is called energy backscattering. Energy backscattering has been observed experimentally by Bandi *et al.* (2006). These authors further observed that the probability of backscattering increases as the measurement domain of the flow decreases, which is consistent with the numerical finding by Tao, Katz & Meneveau (2002). In the present study the decrease of aspect ratio also reduces the size of averaging flow domains. Moreover, as the aspect ratio decreases turbulent flows becomes increasingly anisotropic and quasi-2-D; it would therefore be interesting to examine how this influences energy backscattering.

We first check the convergence of the third-order structure function by examining its integral kernels for three different separations r, representative of the dissipative, the inertial and the largest length scales. The results are plotted in figure 13, showing that the integrals are finite, since the integral kernels approach zero for large values of $\delta_r u_r$.

Figure 14 shows examples of the locally-averaged energy dissipation rate as a function of r averaged over a centre volume of the RB convection cell with $Ra = 1 \times 10^9$, $Pr = 4.38$ and aspect ratios $\Gamma = 1$ and $1/8$. It can be seen that the energy flux is always positive, which is evidence for a direct energy cascade. For $\Gamma = 1$ the energy flux is almost constant for the largest scales until $r \approx 10\eta_k$ is reached and the energy flux begins to vanish rapidly, indicating that the energy is dissipated by small scales. In this case the inertial range covers only about $\Delta r = L_{11} - 10\eta_k \approx 0.1$ cell heights, where L_{11} is the longitudinal integral scale. For $\Gamma = 1/8$ the r-distribution of the energy flux looks slightly different with a clear maximum at approximately $r \approx 20\eta_k$ and generally slightly higher values of $\epsilon_{centre}(r)$. Since the integration volume for $\Gamma = 1/8$ is only $1/8$ of the volume used for $\Gamma = 1$, we also compute the flux in the cubic cell using the same subvolume as in the $\Gamma = 1/8$ case. Figure 14(*c*) shows that the maximum value of $\epsilon_{centre}(r)$ in this case is about the same as in figure 14(*a*), suggesting that the extent of the integration volume in the y direction does not have

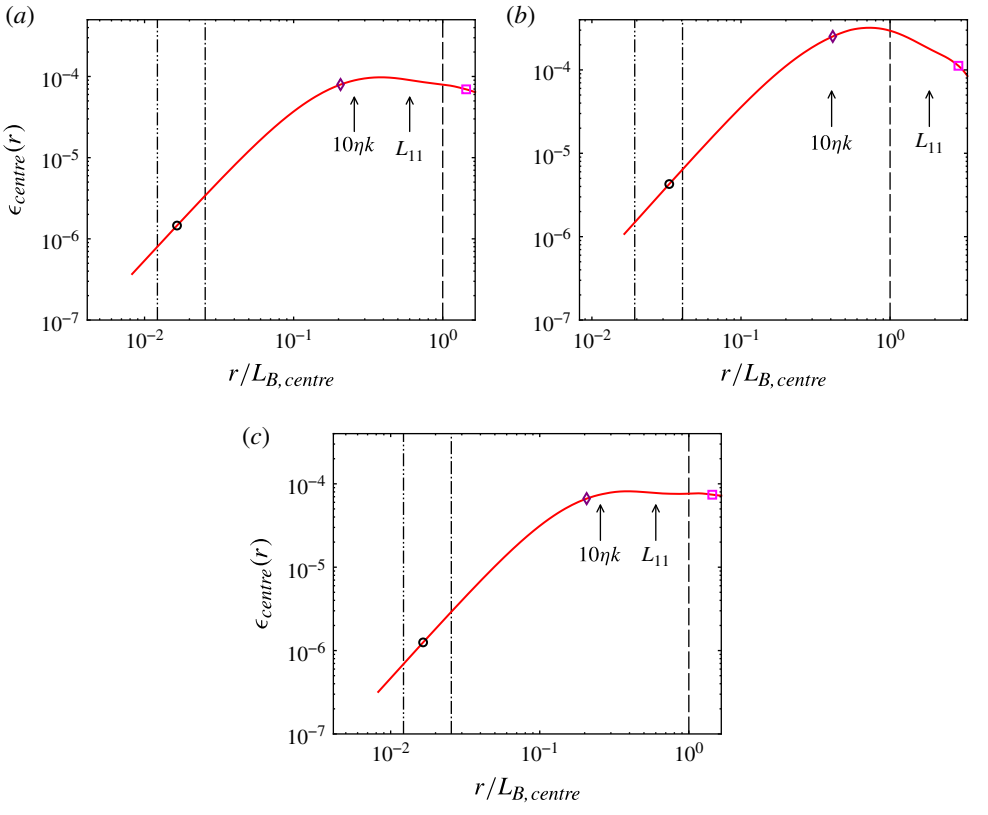

FIGURE 14. (Colour online) The energy flux $\epsilon_{centre}(r) = \langle(\delta_r u_r)^3\rangle_{centre,t}/(-4/5r)$ evaluated in the centre of the cell for $Ra = 1 \times 10^9$ and $Pr = 4.38$ for (*a*) $\Gamma = 1$ and (*b*) $\Gamma = 1/8$. The vertical lines represent the Batchelor length scale η_b (-···-), the Kolmogorov length scale (···) and the local Bolgiano length scale $L_{B,centre}$ (– –) averaged over the centre of the cube ($V_{centre} = \Gamma 0.5^3$). Panel (*c*) shows $\epsilon_{centre}(r)$ evaluated in the cube, but using the same subvolume as for the $\Gamma = 1/8$ cell. The symbols indicate the r values used in figure 15 in the dissipative range (circles), in the lower end of the inertial range (diamonds) and at large scale (squares). The arrows indicate the region where the inertial range is to expected (L_{11} is the longitudinal integral scale).

a significant effect on $\epsilon_{centre}(r)$, hence confirming the different cascade processes in the cubic and $\Gamma = 1/8$ geometries. Another feature that can be seen from the figure is that the inertial range is now much wider. This is an indication that the turbulent flow in the smaller averaging volume is now more homogeneous and isotropic, as the averaging volume now encloses only a small region in the central core. We note that the maximum value of $\epsilon_{centre}(r)$ in all these cases occurs near the Taylor microscale. We also computed the energy flux for our small-aspect-ratio shear-free simulations and observed that its shape is qualitatively the same as in figure 14(*b*).

Figure 15 shows the p.d.f.s of the instantaneous energy flux $\epsilon_{centre}(r, t)$ for three different length scales r as indicated by the symbols in figure 14, i.e. r values that are in the dissipative range, at the lower end of the inertial range, and at the largest scales, respectively. It is seen clearly that, due to its small averaging volume and quasi-2-D nature, there exists stronger energy backscattering, as shown by the negative

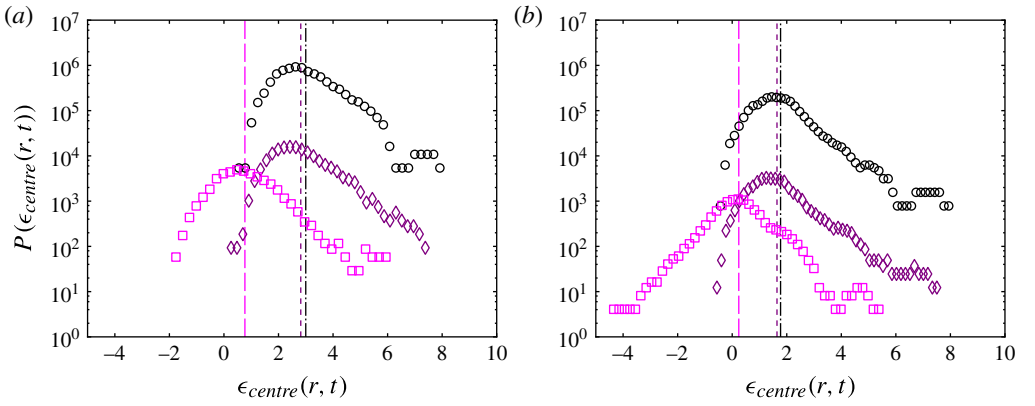

FIGURE 15. (Colour online) The p.d.f.s of the energy flux $\epsilon_{centre}(r,\ t) = \langle(\delta_r u_r(r,t))^3\rangle_{centre}/(-4/5r)$ evaluated in the centre of (*a*) the $\Gamma = 1$ cell (corresponding to the case in figure 14*a*) and (*b*) the $\Gamma = 1/8$ cell (corresponding to the case in figure 14*b*), for $Ra = 1 \times 10^9$ and $Pr = 4.38$. Different symbols represent the values of the scale r as indicated in figure 14 and the vertical lines represent the respective mean values.

energy flux, in the $\Gamma = 1/8$ geometry than in the $\Gamma = 1$ case, i.e. the momentary reversals of the energy cascade direction now occur more frequently, even though the overall energy flux is still positive, as indicated by the mean values. It should also be noted that there is now backscattering even for r at large scales, and the mean values are also smaller. These findings are consistent with those by Tao *et al.* (2002) and Bandi *et al.* (2006). Furthermore, in $\Gamma = 1/8$ and for r in the dissipative range, the distribution is almost symmetric with the mean close to zero. Normalization with their respective r.m.s. values, however, yields very similar distributions of $\epsilon_{centre}(r,\ t)$ in both geometries.

5. Effect of bulk resolution on the small-scale properties

In the course of our study we encountered the problem that there seem to be quantities that scale differently with Ra in a cube than in a cylindrical geometry. Since we did not know *a priori* which differences are physical and which might be errors of the simulation, whether due to the finite averaging time, contamination by transients or under-resolution, we had to rule out at least the most obvious ones, so we increased the resolution and waited for a longer time before starting to average. In the following an example of the influence of the bulk resolution is given by comparing two such grids, one with low and one with high resolution.

Typically, the Nusselt number Nu is computed in different ways using a spatial average over horizontal slices and volume averages of the turbulent kinetic energy dissipation rate and the temperature variance dissipation rate to test the resolution, which we have also presented in table 1. It can be seen that the results are all within their error bars. It is, however, important to be aware of the limits of this approach: it applies to integral quantities, but care should be taken when local quantities are investigated. Since we are interested in the small-scale properties of the core region, in particular their scaling with respect to the scale separation r, we believe that a more rigorous check is necessary. We therefore use the second-order longitudinal structure functions, in order to study the impact of the resolution on the dynamics of the bulk flow.

	N_H	N_G	N_S	N_v	N_T	Nu_S	$Nu(\epsilon_u)$	$Nu(\epsilon_T)$	t_{avg}
Simulation 1	898	338	1060	21/12.6	14/7.6	130.6 ± 1.0	131.2 ± 0.9	129.2 ± 0.7	240
Simulation 2	1142	338	1060	19/12.6	13/7.6	130.7 ± 0.5	130.0 ± 0.5	131.5 ± 1.2	80

TABLE 2. Characteristic quantities for the resolution check at $Ra = 1 \times 10^{10}$, $Pr = 4.38$ and $\Gamma = 1/4$. The number of grid points of the simulation in the vertical direction is N_H and the estimates N_G and N_S are from Shishkina *et al.* (2010) and Grötzbach (1983), respectively. The resolutions in the other two directions, $N_x \times N_y$, for simulations 1 and 2 are 770×258 and 1142×326, respectively. Comparison is made of the number of grid points in the viscous and thermal boundary layers N_v and N_T (actual resolution/requirement), the mean Nusselt number Nu_S calculated by averaging over horizontal slices and through volume averages of the kinetic and thermal dissipation rates and the averaging time t_{avg}.

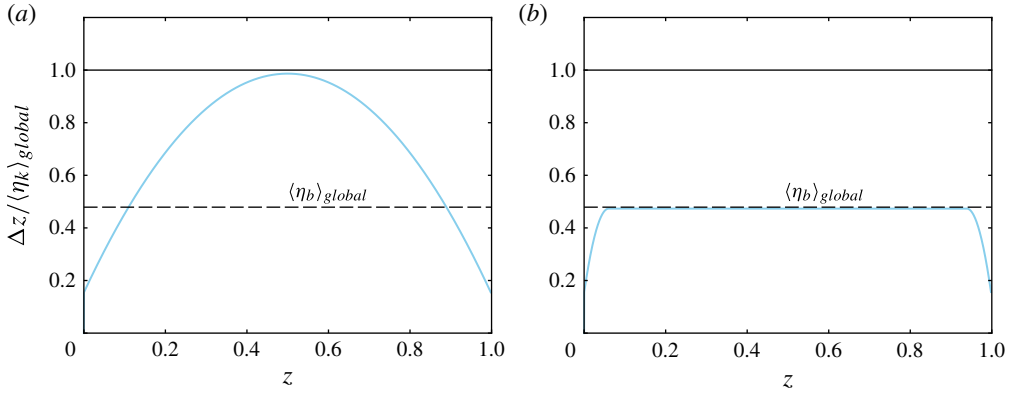

FIGURE 16. (Colour online) The vertical grid spacing as a function of the vertical coordinate for (*a*) simulation 1 with $N_H = 898$ grid points and (*b*) simulation 2 with $N_H = 1142$ grid points. The grids are designed for $Ra = 1 \times 10^{10}$ and $Pr = 4.38$.

In table 2 some general information on the resolution requirements is provided and in figure 16 the actual grids are illustrated. The grid for simulation 1 is designed in such a way that the local grid spacing is always smaller than the global estimate of the Kolmogorov length scale, while the grid for simulation 2 is designed with a grid spacing that is always smaller than the global estimate of the Batchelor length scale. Knowing that the local dissipative length scales in the bulk are larger than their global estimates, the first grid will resolve the Kolmogorov scales very well, while the second one will also resolve the Batchelor length scales very well.

In figure 17 we compare the second-order longitudinal vertical velocity structure functions $\langle\delta_r w\rangle_{centre}$ averaged in time and over the core region of both simulations, revealing that despite the (mean) Kolmogorov scales of both simulations being resolved, both structure functions differ. Comparison of the temperature structure functions shows an even clearer discrepancy between the two simulations. While the high-resolution simulation is close to the analytical r^2 scaling in the dissipative range, figure 18 reveals that the lower-resolution case does not obey the r^2 scaling in the dissipative range.

In order to quantify our observations, we compute the exponent of r for both simulations and find that $\langle\delta_r w\rangle \sim r^{1.98}$ and $\langle\delta_r w\rangle \sim r^{1.99}$ for simulations 1 and 2,

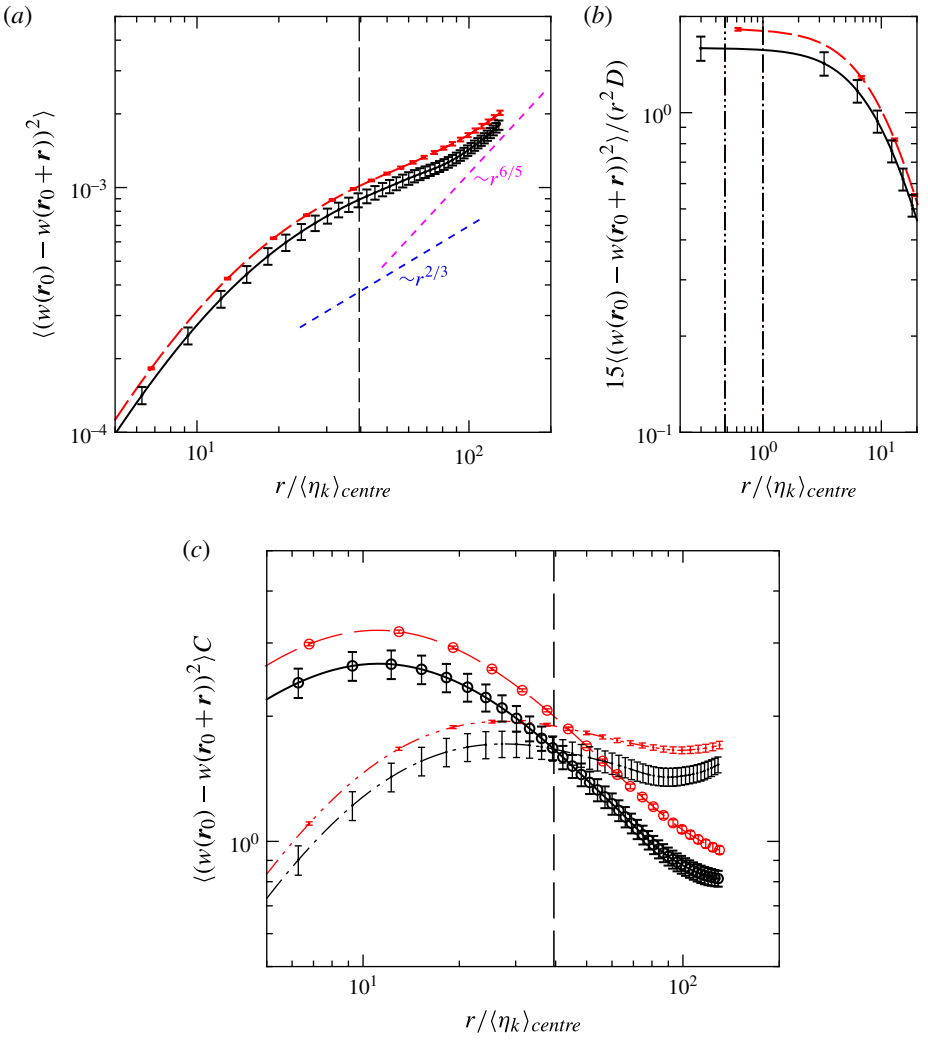

FIGURE 17. (Colour online) (*a*) The second-order longitudinal structure functions of vertical velocity increments for simulation 1 with $N_H = 898$ grid points in the vertical direction (- -) and simulation 2 with $N_H = 1142$ grid points (—) in the vertical direction. The scalings of the dissipative range $\langle\delta_r w\rangle \sim r^2$, the K41 scaling ($\langle\delta_r w\rangle \sim r^{2/3}$) and the BO59 scaling ($\langle\delta_r w\rangle \sim r^{6/5}$) of the inertial range are given for reference. (*b*) The r^2-compensated plots of the structure functions normalized with $D = \langle\epsilon_u\rangle_{centre}(Ra/Pr)^{1/2}$. The vertical lines indicate the positions of the local Batchelor length scale $\langle\eta_b\rangle_{centre}$ (–··–), the local Kolmogorov length scale $\langle\eta_k\rangle_{centre}$ (–·–) and the local Bolgiano length scale $L_{B,centre}$ (– –). (*c*) The BO59-compensated (– – $N_H = 898$; — $N_H = 1142$; $C = r^{-6/5}\langle\epsilon_T\rangle_{centre}^{-2/5}$) and K41-compensated (-··· $N_H = 898$; –·– $N_H = 1142$; $C = r^{-2/3}\langle\epsilon_u\rangle_{centre}^{-2/3}$) structure functions.

respectively, which we consider to be good approximations of the dissipative range. For the temperature structure function we observe the scalings $\langle\delta_r T\rangle \sim r^{1.80}$ and $\langle\delta_r T\rangle \sim r^{1.95}$ for the respective simulations. This indicates that not enough thermal energy is dissipated in this area of the flow. Since both simulations run stably and yield similar global *Nu* values, this also raises the question of how under-resolving

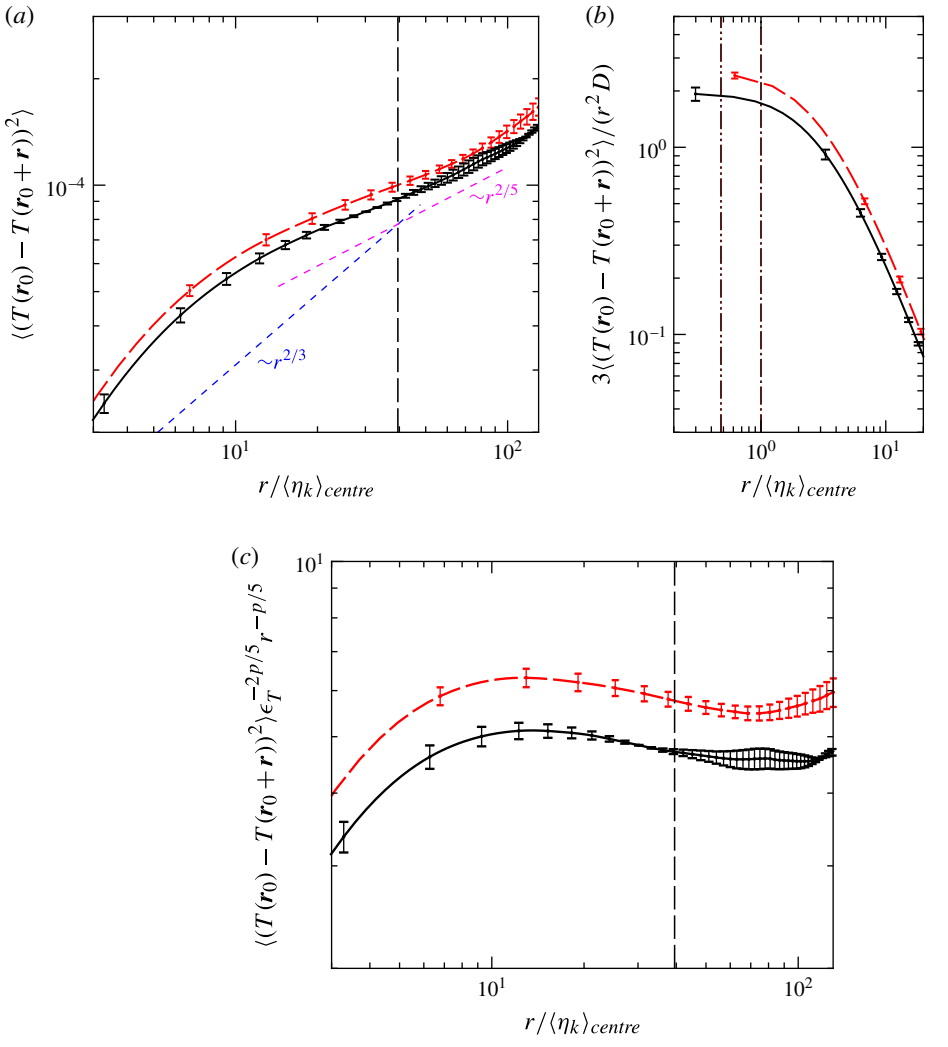

FIGURE 18. (Colour online) (*a*) The second-order temperature structure functions of vertical temperature increments for simulation 1 with $N_H = 898$ grid points (- -) and simulation 2 with $N_H = 1142$ grid points (—). The scalings of the dissipative range $\langle \delta_r T \rangle \sim r^2$, the K41 scaling ($\langle \delta_r T \rangle \sim r^{2/3}$) and the BO59 scaling ($\langle \delta_r T \rangle \sim r^{2/5}$) of the inertial range are given for reference. (*b*) The r^2-compensated plots of the structure functions normalized with $D = \langle \epsilon_T \rangle_{centre} (RaPr)^{1/2}$. (*c*) The BO59-compensated structure functions. The vertical lines indicate the positions of the local Batchelor length scale $\langle \eta_b \rangle_{centre}$ (–·–), the local Kolmogorov length scale $\langle \eta_k \rangle_{centre}$ (–·–) and the local Bolgiano length scale $L_{B,centre}$ (– –).

the bulk might affect other regions of the flow, namely the boundary layers, which need to dissipate this excess of thermal energy.

At first sight, the poor performance of simulation 2 might come as a surprise, since both $\langle \eta_b \rangle_{centre}$ and $\langle \eta_k \rangle_{centre}$ are well resolved. Since it is known that plumes intermittently penetrate the bulk and thermal plumes are in effect detached thermal boundary layers, it also becomes clear that, strictly speaking, boundary-layer resolution would be necessary to resolve all relevant turbulent scales in the bulk, a requirement

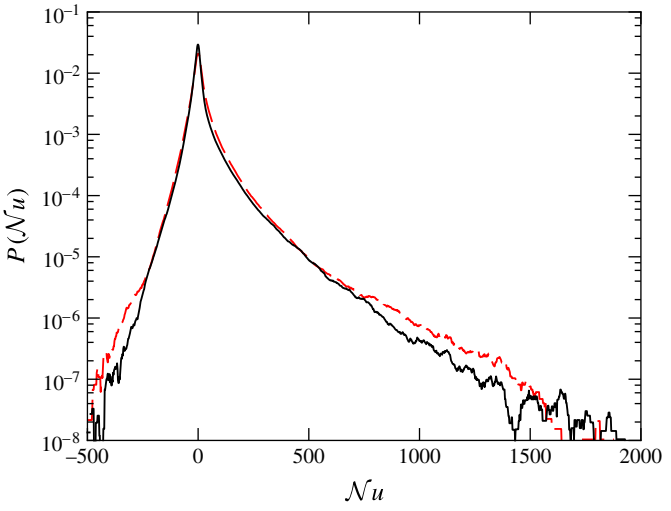

FIGURE 19. (Colour online) The p.d.f.s of the heat flux through the bulk region ($V = \Gamma(0.25H)^3$) for simulation 1 with $N_H = 898$ grid points (- -) and simulation 2 with $N_H = 1142$ grid points (—). The mean convective heat flux is $Nu_{centre} = 9.0 \pm 2.0$ ($N_H = 898$) and $Nu_{centre} = 10.4 \pm 0.3$ ($N_H = 1142$).

that given the present computational resources is not practical. In the range of Ra and Pr considered here, the scaling exponent of the thermal-boundary-layer thickness with Ra is approximately -0.3 and the local dissipative scale in the boundary layer can be estimated to follow the Ra scaling $\eta_{k,BL} \sim (Nu^{0.3})^{-3/2}$ (see (39)–(41) in Shishkina *et al.* (2010)). The local Kolmogorov length scale in the bulk scales as $\langle \eta_k \rangle_{centre} \sim Ra^{-3/8}$, which follows from $\langle \eta_k \rangle_{centre} = [(Ra/Pr)^{3/2} \langle \epsilon_u \rangle_{centre}]^{-1/4}$ and $\langle \epsilon_u \rangle_{centre} \approx$ const for high Ra (see the data of Ni *et al.* (2011) plotted in Kaczorowski & Xia 2013). Following the above way of resolving the bulk, this yields a resolution deficit of the thermal plumes that scales as $\eta_{k,BL}/\langle \eta_k \rangle_{centre} \sim Ra^{-0.08}$, showing that adequate resolution of the bulk becomes increasingly challenging or, in other words, as the flow becomes more and more intermittent at high Ra the numerical errors will dramatically increase if the meshes are not designed accordingly.

Furthermore, we investigate the impact of the resolution on the p.d.f. of the local convective heat flux in the centre of the cell. Figure 19 illustrates that both p.d.f.s have a very similar shape, with the tails of the low-resolution p.d.f. being slightly higher than the tails of the high-resolution case. Integration of the two p.d.f.s yields that the mean convective heat fluxes through the centre of the cell are within the error bars of the simulations: $Nu_{centre} = 9.0 \pm 2.0$ with $N_H = 898$ versus $Nu_{centre} = 10.4 \pm 0.3$ with $N_H = 1142$.

6. Conclusions

We have extended our highly-resolved direct numerical simulation study (Kaczorowski & Xia 2013) on the small-scale properties of turbulent RBC in the core region of a cubic cell by investigating the impact of lateral confinement on the small-scale statistics in the bulk, and hence have also complemented our study on confinement-induced heat transfer enhancement (Huang *et al.* 2013), which is concerned with the aspect-ratio dependence of the large-scale flow features.

We find that the local Bolgiano length scale in the bulk of turbulent RBC can be reduced by geometrically confining the flow in the lateral direction of the cell. It is observed that the rate at which the local Bolgiano length scale in the centre of the cell decreases with decreasing Γ is larger for $Pr = 0.7$ than for $Pr = 4.38$. This affords one the opportunity to investigate the influence of the local Bolgiano length scale on cascade processes at any Ra and Pr by simply varying Γ. The local energy flux in the centre of the cell calculated as $\epsilon_{centre}(r, t) = \langle(\delta_r u_r(r, t))^3\rangle_{centre}/(-4/5r)$ is shown to vary significantly for separations $r \gtrapprox 10\eta_k$, where the $\Gamma = 1$ cell exhibits a plateau, while the $\Gamma = 1/8$ cell forms a clear maximum, revealing the impact of lateral confinement on the cascade processes in the bulk region. However, unlike the findings by Boffetta *et al.* (2012) in developing Rayleigh–Taylor turbulence, the local Bolgiano length scale in the centre of turbulent RBC is not strictly confined by the smallest dimension of the container. We do, however, observe that the local Bolgiano length scale in the centre of the cell roughly follows the scaling $L_{B,centre} \sim W_y$, when Γ is smaller than a certain value, which imposes a cut-off on $L_{B,centre}$, which is of the order of the cell's width.

It is also observed that geometrical confinement changes the topology of the flow, since the LSC becomes less stable, which results in more vertical flow through the core region at lower aspect ratios. Hence, the turbulent kinetic energy dissipation rate and the temperature variance dissipation rate, as well as the velocity and temperature fluctuations, increase in the core region until a certain Γ is reached. This mechanism strongly depends on the relative width of the cell compared to the thicknesses of the boundary layers on the lateral walls. This leads to an increased local heat flux, which is also reflected by an increasingly more exponential right tail of the heat flux p.d.f.s of the vertical velocity fluctuations; moreover, in contrast, the p.d.f.s of the temperature fluctuations become almost Gaussian for small aspect ratios.

It is also found that the heat flux through the core region increases as the aspect ratio Γ decreases and that for aspect ratios smaller than unity the local heat flux and the turbulent kinetic energy dissipation rate are balanced, as experimentally observed in the centre of cylindrical geometries. This highlights that (at least for the moderate Rayleigh numbers studied here) there are significant differences between the flows in the core regions of cylindrical and Cartesian geometries that are not yet well understood and require further attention. Furthermore, flow visualizations show that the dynamics of the core region of RBC are strongly geometry dependent, as the bulk flow is stirred by the LSC for large aspect ratios but frequently penetrated by the thermal plumes at small aspect ratios. We also find that, with decreasing Γ, i.e. as the system changes from 3-D to quasi-2-D, the local energy flux $\epsilon_{centre}(r, t)$ in the centre of the cell exhibits an increasing amount of energy backscattering. This backscattering seems to occur at all length scales, but is more significant at small scales.

By analysing the second-order structure functions of the vertical velocity and temperature in the bulk of RBC with $Ra = 1 \times 10^{10}$, $Pr = 4.38$ and $\Gamma = 1/4$, we have shown that under-resolution of the temperature field yields a large error in the dissipative range scaling, resulting in a scaling $\langle\delta_r T\rangle/r^2 \neq \text{const}$. This is thought to be an effect of the thermal plumes (and the related strong gradients at their boundaries) that intermittently propagate through the bulk and essentially require boundary-layer resolution. It is therefore pointed out that the resolution contrast resulting from the requirement to resolve the thermal plumes and the homogeneous and isotropic background turbulence scales as $\delta_T/\langle\eta_k\rangle_{centre} \sim Ra^{0.1}$ and therefore should be taken into account when tackling very high Ra. It is also observed that the p.d.f.s of the

heat flux in the centre of the cell almost coincide for both resolutions, and integration of the p.d.f.s yields that the local vertical heat fluxes of both simulations are within their error bars.

Acknowledgements

This work is supported in part by the Hong Kong Research Grants Council (RGC) under Grant No. CUHK 403712 and in part by the NSFC/RGC Joint Research Scheme under Grant No. N_CUHK462/11. M.K. acknowledges financial support by the EU Science and Technology Fellowship Programme China. This research was conducted using the resources of the Chinese University of Hong Kong's Information and Technology Service Centre and the High Performance Cluster Computing Centre, Hong Kong Baptist University, which receives funding from the Research Grant Council, University Grant Committee of the HKSAR and Hong Kong Baptist University and the Leibnitz Rechenzentrum Munich under project number pr63ro.

Supplementary movie

A supplementary movie is available at http://dx.doi.org/10.1017/jfm.2014.154.

REFERENCES

AHLERS, G., GROSSMANN, S. & LOHSE, D. 2009 Heat transfer & large-scale dynamics in turbulent Rayleigh–Bénard convection. *Rev. Mod. Phys.* **81** (2), 503–537.

BAILON-CUBA, J., EMRAN, M. S. & SCHUMACHER, J. 2010 Aspect ratio dependence of heat transfer and large-scale flow in turbulent convection. *J. Fluid Mech.* **655**, 152–173.

BANDI, M. M., GOLDSTEIN, W. I., CRESSMAN, J. R. & PUMIR, A. 2006 Energy flux fluctuations in a finite volume of turbulent flow. *Phys. Rev.* E **73**, 026308.

BOFFETTA, G., DE LILLO, F., MAZZINO, A. & MUSACCHIO, S. 2012 Bolgiano scale in confined Rayleigh–Taylor turbulence. *J. Fluid Mech.* **690**, 426–440.

CALZAVARINI, E., TOSCHI, F. & TRIPICCIONE, R. 2002 Evidences of Bolgiano scaling in 3D Rayleigh–Bénard convection. *Phys. Rev.* E **66**, 016304.

CELANI, A., MUSACCHIO, S. & VINCENZI, D. 2010 Turbulence in more than two and less than three-dimensions. *Phys. Rev. Lett.* **104**, 184506.

CHILLÀ, F. & SCHUMACHER, J. 2012 New perspectives in turbulent Rayleigh–Bénard convection. *Eur. Phys. J.* E **35**, 1–25.

CHING, E. S. C. 2000 Intermittency of temperature field in turbulent convection. *Phys. Rev.* E **61**, R33–R36.

DUCHON, J. & ROBERT, R. 2000 Inertial energy dissipation for weak solutions of incompressible Euler and Navier–Stokes equations. *Nonlinearity* **13**, 249–255.

EMRAN, M. & SCHUMACHER, J. 2012 Conditional statistics of thermal dissipation rate in turbulent Rayleigh–Bénard convection. *Eur. Phys. J.* E **35**, 1–8.

EYINK, G. L. 2003 Local 4/5-law and energy dissipation anomaly in turbulence. *Nonlinearity* **16**, 137–145.

FUNFSCHILLING, D., BODENSCHATZ, E. & AHLERS, G. 2009 Search for the 'ultimate state' in turbulent Rayleigh–Bénard convection. *Phys. Rev. Lett.* **103**, 014503.

FUNFSCHILLING, D., BROWN, E., NIKOLAENKO, A. & AHLERS, G. 2005 Heat transport by turbulent Rayleigh–Bénard convection in cylindrical samples with aspect ratio one and larger. *J. Fluid Mech.* **536**, 145–154.

GROSSMANN, S. & LOHSE, D. 2003 On geometry effects in Rayleigh–Bénard convection. *J. Fluid Mech.* **486**, 105–114.

GRÖTZBACH, G. 1983 Spatial resolution requirements for direct numerical simulation of Rayleigh–Bénard convection. *J. Comput. Phys.* **49**, 241–264.

HE, X., TONG, P. & CHING, E. 2010 Statistics of the locally averaged thermal dissipation rate in turbulent Rayleigh–Bénard convection. *J. Turbul.* **11**, 1–10.

HUANG, S.-D., KACZOROWSKI, M., NI, R. & XIA, K.-Q. 2013 Confinement induced heat transport enhancement in turbulent thermal convection. *Phys. Rev. Lett.* **111**, 104501(1-5).

KACZOROWSKI, M. & WAGNER, C. 2009 Analysis of the thermal plumes in turbulent Rayleigh–Bénard convection based on well-resolved numerical simulations. *J. Fluid Mech.* **618**, 89–112.

KACZOROWSKI, M. & XIA, K.-Q. 2013 Turbulent flow in the bulk of Rayleigh–Bénard convection: small-scale properties in a cubic cell. *J. Fluid Mech.* **722**, 596–617.

KUNNEN, R. P. J., CLERX, H. J. H., GEURTS, B. J., VAN BOKHOVEN, L. J. A., AKKERMANS, R. A. D. & VERZICCO, R. 2008 Numerical and experimental investigation of structure-function scaling in turbulent Rayleigh–Bénard convection. *Phys. Rev.* E **77**, 016302.

LOHSE, D. & XIA, K.-Q. 2010 Small-scale properties of turbulent Rayleigh–Bénard convection. *Annu. Rev. Fluid Mech.* **42**, 335–364.

NI, R., HUANG, S.-D. & XIA, K.-Q. 2011 Local energy dissipation rate balances local heat flux in the center of turbulent thermal convection. *Phys. Rev. Lett.* **107**, 174503(1-5).

NIEMELA, J. J. & SREENIVASAN, K. R. 2010 Does confined turbulent convection ever attain the 'asymptotic scaling' with 1/2 power? *New J. Phys.* **12**, 115002.

POEL, E. P., STEVENS, R. J. A. M., SUGIYAMA, K. & LOHSE, D. 2012 Flow states in two-dimensional Rayleigh–Bénard convection as a function of aspect ratio and Rayleigh number. *Phys. Fluids* **24**, 085104.

QIU, X.-L. & XIA, K.-Q. 1998 Viscous boundary layers at the sidewall of a convection cell. *Phys. Rev.* E **58**, 486–491.

ROCHE, P. E., CASTAING, B., CHABAUD, B. & HEBRAL, B. 2002 Prandtl and Rayleigh number dependences in Rayleigh–Bénard convection. *Europhys. Lett.* **58**, 693–698.

SHANG, X.-D., QIU, X.-L., TONG, P. & XIA, K.-Q. 2004 Measurements of the local convective heat flux in turbulent Rayleigh–Bénard convection. *Phys. Rev.* E **70**, 026308.

SHANG, X.-D., TONG, P. & XIA, K.-Q. 2008 Scaling of the local convective heat flux in turbulent Rayleigh–Bénard convection. *Phys. Rev. Lett.* **100**, 244503.

SHANG, X.-D. & XIA, K.-Q. 2001 Scaling of the velocity power spectra in turbulent thermal convection. *Phys. Rev.* E **64**, 065301(R).

SHISHKINA, O., STEVENS, R. J. A. M., GROSSMANN, S. & LOHSE, D. 2010 Boundary layer structure in turbulent thermal convection and consequences for the required numerical resolution. *New. J. Phys.* **12**, 075022.

SHISHKINA, O. & WAGNER, C. 2006 Analysis of thermal dissipation rates in turbulent Rayleigh–Bénard convection. *J. Fluid Mech.* **546**, 51–60.

SHISHKINA, O. & WAGNER, C. 2007 Local heat flux in turbulent Rayleigh–Bénard convection. *Phys. Fluids* **19** (8), 085107-1–085107-13.

STEVENS, R. J. A. M., VERZICCO, R. & LOHSE, D. 2010 Radial boundary layer structure and Nusselt number in Rayleigh–Bénard convection. *J. Fluid Mech.* **643**, 495–507.

SUN, C., REN, L.-Y., SONG, H. & XIA, K.-Q. 2005*a* Heat transport by turbulent Rayleigh–Bénard convection in 1 m diameter cyindrical cells of widely varying aspect ratio. *J. Fluid Mech.* **542**, 165–174.

SUN, C., XIA, K.-Q. & TONG, P. 2005*b* Three-dimensional flow structures and dynamics of turbulent thermal convection in a cylindrical cell. *Phys. Rev.* E **72**, 026302(13).

SUN, C., ZHOU, Q. & XIA, K.-Q. 2006 Cascades of velocity and temperature fluctuations in buoyancy-driven thermal turbulence. *Phys. Rev. Lett.* **97**, 144504.

TAO, B., KATZ, J. & MENEVEAU, C. 2002 Statistical geometry of subgrid-scale stresses determined from holographic particle image velocimetry measurements. *J. Fluid Mech.* **457**, 35–78.

XIA, K.-Q. 2013 Current trends and future directions in turbulent thermal convection. *Theor. Appl. Mech. Lett.* **3**, 052001(1-12).

XIN, Y.-B. & XIA, K.-Q. 1997 Boundary layer length scales in convective turbulence. *Phys. Rev.* E **56**, 3010–3015.

ZHOU, Q., LIU, B.-F., LI, C.-M. & ZHONG, B.-C. 2012 Aspect ratio dependence of heat transport by turbulent Rayleigh–Bénard convection in rectangular cells. *J. Fluid Mech.* **710**, 260–276.

ZHOU, S.-Q. & XIA, K.-Q. 2001 Scaling properties of the temperature field in convective turbulence. *Phys. Rev. Lett.* **87**, 064501.

ZHOU, Q. & XIA, K.-Q. 2008 Comparative experimental study of local mixing of active and passive scalars in turbulent thermal convection. *Phys. Rev.* E **77**, 056312.

ZHOU, Q. & XIA, K.-Q. 2010 Universality of local dissipation scales in buoyancy-driven turbulence. *Phys. Rev. Lett.* **104**, 124301.